

# A General Method for Constructing Two-Dimensional Layered Mesoporous Mono- and Binary-Transition-Metal Nitride/Graphene as an Ultra-Efficient Support to Enhance Its Catalytic Activity and Durability for Electrocatalytic Application

Baocang Liu,<sup>†,‡</sup> Lili Huo,<sup>†,‡</sup> Rui Si,<sup>\*,§</sup> Jian Liu,<sup>||</sup> and Jun Zhang<sup>\*,†,‡</sup>

<sup>†</sup>College of Chemistry and Chemical Engineering, Inner Mongolia University, Hohhot 010021, P.R. China

<sup>‡</sup>Inner Mongolia Key Lab of Nanoscience and Nanotechnology, Inner Mongolia University, Hohhot 010021, P.R. China

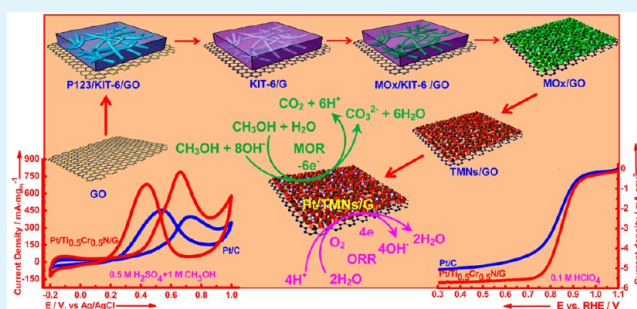
<sup>§</sup>Shanghai Synchrotron Radiation Facility, Shanghai Institute of Applied Physics, Chinese Academy of Sciences, Shanghai 201204, P.R.China

<sup>||</sup>Department of Chemical Engineering, Curtin University, Perth, Western Australia 6102, Australia

## Supporting Information

**ABSTRACT:** We constructed a series of two-dimensional (2D) layered mesoporous mono- and binary-transition-metal nitride/graphene nanocomposites (TMN/G, TM = Ti, Cr, W, Mo, TiCr, TiW, and TiMo) via an efficient and versatile nanocasting strategy for the first time. The 2D layered mesoporous TMN/G is constituted of small TMN nanoparticles composited with graphene nanosheets and has a large surface area with high porosity. Through decoration with well-dispersed Pt nanoparticles, 2D layered mesoporous Pt/TMN/G catalysts can be obtained that display excellent catalytic activity and stability for methanol electro-oxidation reactions (MOR) and oxygen reduction reactions (ORR) in both acidic and alkaline media. The 2D layered mesoporous binary-Pt/TMN/G catalysts possess catalytic activity superior to that of mono-Pt/TMN/G, graphene free Pt/TMN, Pt/G, and Pt/C catalysts. Encouragingly, the 2D layered mesoporous Pt/Ti<sub>0.5</sub>Cr<sub>0.5</sub>N/G catalyst exhibits the best electrocatalytic performance for both MOR and ORR. The outstanding electrocatalytic performance of the Pt/Ti<sub>0.5</sub>Cr<sub>0.5</sub>N/G catalyst is rooted in its large surface area, high porosity, strong interaction among Pt, Ti<sub>0.5</sub>Cr<sub>0.5</sub>N, and graphene, an excellent electron transfer property facilitated by N-doped graphene, and the small size of Pt and Ti<sub>0.5</sub>Cr<sub>0.5</sub>N nanocrystals. The outstanding catalytic performance provides the 2D layered mesoporous Pt/Ti<sub>0.5</sub>Cr<sub>0.5</sub>N/G catalyst with a wide range of application prospects in direct methanol fuel cells in both acidic and alkaline media. The synthetic method may be available for constructing other 2D layered mesoporous metal nitrides, carbides, and phosphides.

**KEYWORDS:** 2D layered structure, mesoporous materials, transition-metal nitride, graphene, electrocatalysis



## 1. INTRODUCTION

Direct methanol fuel cells (DMFCs) and metal-air batteries, as efficient, clean, and promising power sources, have attracted extensive attention due to their low operating temperature, high energy density, and simple structure.<sup>1,2</sup> Pt and Pt-based nanomaterials have been widely used as anode electrode materials of DMFCs to catalyze methanol oxidation reactions and as cathode electrode materials of fuel cell and metal-air batteries to catalyze oxygen reduction reactions (ORR) because of their unique catalytic activity.<sup>3–6</sup> However, the significantly high cost, poor Pt utilization, inferior durability, and low poison resistance of Pt and Pt-based catalysts are the main barriers for commercialization of DMFCs and metal-air battery technology.<sup>7–11</sup> Pt-supported catalysts can enhance catalytic activity, reduce the amount of Pt, and increase Pt utilization, thus displaying a bright application prospect.<sup>12–14</sup> Currently, a

variety of carbon materials such as carbon black,<sup>15</sup> carbon nanotubes,<sup>16,17</sup> and graphene<sup>18,19</sup> have been widely used as supports in Pt-supported catalysts due to their large surface area and outstanding electronic conductivity. However, mass activity and long-term durability of the carbon-supported catalysts are still not satisfactory because of the weak interaction between Pt nanoparticles and supports and poor corrosion resistance performance in acid media.<sup>20,21</sup> Thus, it is necessary to find novel noncarbon-based supports to further improve the catalytic activity and stability of the catalysts used in fuel cells and metal-air batteries in both acidic and alkaline media.<sup>12</sup>

Received: March 28, 2016

Accepted: June 30, 2016

Published: June 30, 2016

Recently, transition-metal nitrides (TMN), especially chromium nitride (CrN) and titanium nitride (TiN), have been proven to be ideal catalyst supports for DMFCs and metal-air batteries because of their high electrical conductivity, outstanding thermal and electrochemical stability, exceptional hardness and corrosion resistance, and good catalyst–support interaction.<sup>12,22–26</sup> It was revealed that Pt/TiN and Pt/CrN catalysts exhibited enhanced catalytic activity and stability compared with those of traditional Pt-supported carbon catalysts in both acidic and alkaline media. This suggests that TMN have great potentials as substitutes to carbon supports.<sup>12</sup> Moreover, it is well-known that the size, morphology, and porosity of supports and catalysts may have significant influence on their electrocatalytic performance, and smaller size and larger porosity and surface area are beneficial for improving their catalytic performance.<sup>27,28</sup> For TMN supports, reducing the size by homogeneously dispersing them on the supports<sup>29–31</sup> and increasing the porosity and surface area through endowing a mesoporous structure<sup>24–26</sup> are the two most efficient ways to improve their catalytic activity and stability. For instance, Fu's group reported the synthesis of small-size WN nanoparticles loaded on GO-derived graphene, which can be used as a promising carrier of Pt for MOR with enhanced catalytic activity, excellent resistance to CO poisoning, and durability due to small size and high dispersion of WN nanoparticles.<sup>29</sup> DiSalvo's group prepared mesoporous CrN via ammonolysis of a bulk ternary oxide (K<sub>2</sub>Cr<sub>2</sub>O<sub>7</sub>), and after loading Pt nanoparticles, the obtained Pt/CrN catalyst displayed both electrocatalytic activity and corrosion resistance higher than those of conventional Pt/C catalysts in PEMFCs due to the smaller pore size and higher surface area.<sup>26</sup> Among numerous supports, graphene is the most important one due to its large surface area, excellent electrical conductivity, and low cost.<sup>32</sup> However, the most studied graphene-supported TMN and mesoporous TMN are monometal nitrides.<sup>31,26,33,34</sup>

Very recently, binary-TMN have become a focus of study due to the enhanced synergy effect of two transition-metal components available for promoting the electrocatalytic activity and durability.<sup>35–38</sup> However, most binary-TMN were synthesized via a simple precursor-pyrolytic process, and the size and porosity of TMN are usually uncontrollable.<sup>35,36</sup> Moreover, at present, the most-studied TMN are either supported on graphene and other carbons or on an individually adopted mesoporous structure. The integration of mesoporous TMN with graphene has been rarely reported. Thus, development is urgently required of a controllable synthetic method to prepare TMN/G with large surface area, good electron transportation properties, ultrafine TMN nanoparticle distribution, and strong synergetic effects between graphene and binary-transition-metal nitrides by combining three components of graphene, binary-TMN, and mesoporous configuration together and integrating their individual superiority to further promote their electrocatalytic activity and durability. It is predicted that combining graphene with mesoporous TMN to form 2D layered mesoporous TMN/G nanocomposites possessing the small size, large porosity, and good electrical conductivity of TMN will further improve the electrocatalytic activity and stability.

Herein, we developed a general route to synthesize a series of 2D layered mesoporous mono- and binary-TMN/G nanocomposites with large surface area, high porosity, and good electrical conductivity. Among of them, the 2D layered mesoporous binary Ti<sub>0.5</sub>Cr<sub>0.5</sub>N/G nanocomposites display the

optimum electrocatalytic property. After being loaded with Pt nanoparticles, the 2D layered mesoporous Pt/Ti<sub>0.5</sub>Cr<sub>0.5</sub>N/G catalysts exhibit electrocatalytic activity and durability much higher than those of traditional Pt/C, Pt/G, mono-Pt/TiN/G, mono-Pt/CrN/G, and graphene-free binary-Pt/TiCrN catalysts toward MOR and ORR due to the improved exposure of active sites, enhanced mass transfer efficiencies, large accessible active sites, and excellent electron-transport property. To the best of our knowledge, this is the first report on the construction of 2D layered mesoporous Pt/TMN/G catalysts with superior electrocatalytic activity and durability as MOR and ORR catalysts for high-performance DMFCs in both acidic and alkaline media.

## 2. EXPERIMENTAL SECTION

**2.1. Materials and Synthesis. Chemicals.** Cr(NO<sub>3</sub>)<sub>3</sub>·9H<sub>2</sub>O (analytical reagent (AR), ≥99%), tetrabutyl titanate (TBOT, CR, ≥99%), tetraethyl orthosilicate (TEOS, AR, ≥96%), HCl (AR, 37 wt %), H<sub>2</sub>SO<sub>4</sub> (AR, 98 wt %), H<sub>3</sub>PO<sub>4</sub> (AR, ≥85%), H<sub>2</sub>O<sub>2</sub> (AR, 30%), H<sub>2</sub>PtCl<sub>6</sub> (AR, Pt ≥ 37.5%), and NaOH (AR) were obtained from Sinopharm Chemical Reagent Co., Ltd. Ammonium molybdate (NH<sub>4</sub>)<sub>6</sub>Mo<sub>7</sub>O<sub>24</sub>·4H<sub>2</sub>O, AR, ≥99.0%), 12-tungstophosphoric acid hydrate (H<sub>3</sub>(PW<sub>12</sub>O<sub>40</sub>)·xH<sub>2</sub>O, AR, ≥ 99.0%), and graphite powder (AR, 99%) were purchased from J&K Chemical Ltd. Pluronic P123 (Poly(ethylene glycol)-*block*-poly(propylene glycol)-*block*-poly(ethylene glycol), average M<sub>n</sub> ~ 5,800) was obtained from Sigma-Aldrich. Platinum (nominally 20% on carbon black, HiSPEC 3000) was obtained from Alfa Aesar (China). All reagents were used as received without further purification, and all aqueous solutions were prepared with ultrapure water (>18 MΩ·cm) obtained from a Millipore system.

**Synthesis of Graphene Oxide (GO).** Graphene oxide (GO) was prepared by a modified Hummer's method. Typically, 1 g of graphite powder was slowly added into a mixed solution of concentrated sulfuric acid (130 mL) and phosphoric acid (30 mL) containing 6 g of KMnO<sub>4</sub> in a 250 mL ground flask in an ice bath. Then, the flask was transferred to an oil bath and kept at 50 °C for over 12 h under mechanical stirring. After being naturally cooled to ambient temperature, the turbid liquid was slowly poured into a 500 mL beaker containing 15 mL of H<sub>2</sub>O<sub>2</sub> and 100 mL of deionized water with continuous stirring, and the solution in the beaker immediately turned light yellow, indicating the formation of GO. The turbid liquid was completely added and further stirred for 2 h to ensure the complete oxidation of graphite. Subsequently, the obtained yellow turbid liquid was centrifuged at 2000 rpm in a 10 mL tube, and the black particles of unreacted graphite were discarded. The turbid liquid in the top of the tube was washed with concentrated HCl, deionized water, and ethanol three times. After being freeze-dried overnight, GO was obtained.

**Synthesis of the 2D Layered Mesoporous KIT-6/G Template.** KIT-6/G was prepared according to a modified method reported previously.<sup>39</sup> Briefly, 6.0 g of triblock copolymer pluronic P123, 1 g of GO, 6 g of *n*-butanol, and 11.8 g of concentrated HCl were added together into 150 g of aqueous solution and continuously stirred at 45 °C for 24 h. Then, 12 g of TEOS was added to the above solution under vigorous stirring at a speed of 0.5 mL/min. Then, the solution mixture was kept under stirring conditions at 45 °C for another 24 h. After microwave treatment (750 W) for 1 h at 100 °C, dark yellow KIT-6/GO was collected by filtration, washed with water and ethanol, and calcined at 350 °C for 4 h in air.

**Synthesis of 2D Layered Mesoporous Mono- and Binary-Transition-Metal Nitride/Graphene (TMN/G) Nanocomposites.** 2D layered mesoporous mono- and binary-transition-metal nitride/graphene (TMN/G) nanocomposites were prepared using a nanocasting method. With the synthesis of the 2D layered mesoporous mono-CrN/G nanocomposite as an example, the typical synthetic procedures are described as follows: First, 0.8 g of Cr(NO<sub>3</sub>)<sub>3</sub>·9H<sub>2</sub>O was dissolved in 5 mL of deionized water, and then 0.4 g of KIT-6/G template was added. The mixture was stirred for 3 h at room

temperature, and then the deionized water was evaporated at 70 °C until it was completely dried. The collected nanocomposite was calcined at 800 °C for 4 h at a heating rate of 2 °C/min. After the KIT-6 template was removed using a 2 M NaOH aqueous solution at 80 °C followed by several washes with deionized water and drying at 50 °C, the 2D layered mesoporous Cr<sub>2</sub>O<sub>3</sub>/G was achieved. To obtain the 2D layered mesoporous CrN/G nanocomposite, Cr<sub>2</sub>O<sub>3</sub>/G was placed in an alumina boat and heated at 850 °C in a tube furnace at a heating rate of 2 °C/min for 6 h under an ammonia atmosphere to evolve into the 2D layered mesoporous CrN/G nanocomposite. The synthesis of mesoporous TiN/G, WN/G, and Mo<sub>2</sub>N/G nanocomposites followed similar synthetic procedures. For synthesis of the 2D layered mesoporous TiN/G nanocomposite, 0.8 g of Cr(NO<sub>3</sub>)<sub>3</sub>·9H<sub>2</sub>O and 5 mL of deionized water were replaced by 2 mL of TBOT and 10 mL of absolute ethanol. For synthesis of the 2D layered mesoporous WN/G nanocomposite, 0.8 g of Cr(NO<sub>3</sub>)<sub>3</sub>·9H<sub>2</sub>O and 5 mL of deionized water were replaced by 0.6 of phosphotungstic acid and 10 mL of deionized water. When 0.8 g of Cr(NO<sub>3</sub>)<sub>3</sub>·9H<sub>2</sub>O and 5 mL of deionized water are replaced with 0.5 g of ammonium molybdate and 10 mL of deionized water, a 2D layered mesoporous Mo<sub>2</sub>N/G nanocomposite was achieved. Synthesis of the binary-Ti<sub>0.5</sub>Cr<sub>0.5</sub>N/G nanocomposite was slightly varied, and the procedure involved three main steps: 1.0 mL of TBOT dissolved in 10 mL of ethanol was first filled into 0.4 g of KIT-6/G template at room temperature under magnetic stirring followed by several washes with ethanol and drying at 60 °C for 12 h. Then, Cr(NO<sub>3</sub>)<sub>3</sub>·9H<sub>2</sub>O, phosphotungstic acid, and ammonium molybdate were further filled into the above TBOT/KIT-6/G nanocomposite with molar ratios of Cr/Ti, Mo/Ti, and W/Ti fixed at 1:1, 1:4, and 1:4, respectively, to achieve 2D layered mesoporous TiO<sub>2</sub>-Cr<sub>2</sub>O<sub>3</sub>/G, TiO<sub>2</sub>-WO<sub>3</sub>/G, and TiO<sub>2</sub>-MoO<sub>3</sub>/G nanocomposites according to procedures similar to those described above. After nitridation treatment in a NH<sub>3</sub> atmosphere at 850 °C for 6 h, 2D layered mesoporous binary-TiCrN/G, TiWN/G, and TiMoN/G nanocomposites were obtained.

**Synthesis of Pt-Supported 2D Layered Mesoporous Mono- and Binary-Transition-Metal Nitride/Graphene (Pt/TMN/G) Catalysts.** Pt/TMN/G catalysts were prepared by loading Pt nanoparticles on TMN/G via an ethylene glycol (EG) reduction method, and the total Pt loading amount was controlled at ~20 wt %. Typically, 25 mg of 2D layered mesoporous mono- and binary-TMN/G and 1.9 mL of a H<sub>2</sub>PtCl<sub>6</sub>·6H<sub>2</sub>O EG solution (10 mg·mL<sup>-1</sup>) were mixed with 20 mL of EG followed by vigorous stirring and ultrasonication for 1 h at room temperature. Then, the mixture was transferred to a Teflon-lined stainless steel reactor and heated at 140 °C for 3 h. Subsequently, the suspension was centrifuged and washed thoroughly with deionized water and ethanol three times and then dried at 50 °C for 12 h.

**Synthesis of Pt/G Catalyst.** Synthesis of the Pt/G catalyst followed a synthetic procedure similar to that of the mesoporous Pt/TMN/G catalysts except that the TMN/G nanocomposites were replaced by graphene oxide.

**Synthesis of Graphene.** Graphene was obtained via directly calcining graphene oxide at 800 °C under a N<sub>2</sub> atmosphere.

**2.2. Instrumentation.** X-ray diffraction (XRD) was performed on a PANalytical Empyrean diffractometer with Cu K $\alpha$  radiation ( $\lambda = 1.5405 \text{ \AA}$ ) in the Bragg angle ranging between 20° and 80°. Scanning transmission electron microscopy (STEM) and transmission electron microscopy (TEM) characterizations were performed on a FEI Tecnai F20 field-emission transmission electron microscope (FE-TEM). Scanning electron micrographs were recorded with a HITACHI S4800 field-emission scanning electron microscope (FE-SEM). Surface area measurements were performed on an ASAP 2020 Brunauer-Emmett-Teller (BET) analyzer. X-ray photoelectron spectroscopy (XPS) measurements were performed in a VG Scientific ESCALAB Mark II spectrometer equipped with two ultrahigh vacuum (UHV) chambers. The actual Pt content in the catalysts was estimated with a VARIAN VISTA-MPX ICP-Mass spectrometer (MS, United States). The Pt L-III absorption edge ( $E_0 = 11564 \text{ eV}$ ) X-ray absorption fine structure (XAFS) spectra were collected in fluorescence mode by a Lytle ion chamber at the BL14W1 beamline of the Shanghai Synchrotron Radiation Facility (SSRF) operated at 3.5 GeV in “top-

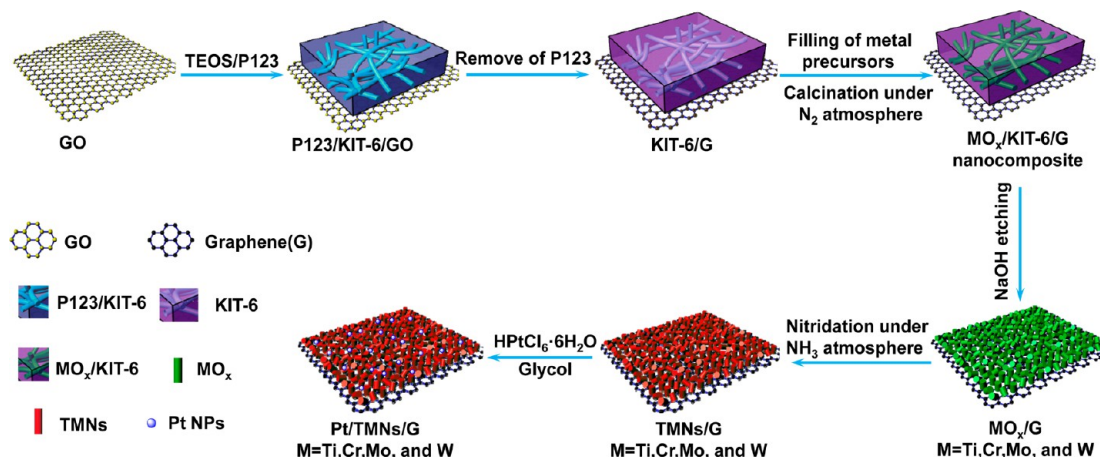
up” mode with a constant current of 240 mA. The energy was calibrated accordingly to the absorption edge of pure Pt foil. Athena and Artemis codes were used to extract the data and fit the profiles. For the X-ray absorption near-edge structure (XANES) part, the experimental absorption coefficients as a function of energies  $\mu(E)$  were processed by background subtraction and normalization procedures. On the basis of the normalized XANES profiles, the chemical valence of platinum in the measured samples can be determined by the help of standards. For the extended X-ray absorption fine structure (EXAFS) part, the Fourier transformed (FT) data in the  $R$  space were analyzed by applying the metallic Pt model for the Pt-Pt shell. The passive electron factors ( $S_0^2$ ) were determined by fitting the experimental Pt foil data and fixing the Pt-Pt coordination number (CN) to be 12 for further analysis of the measured samples. The parameters describing the electronic properties (e.g., correction to the photoelectron energy origin,  $E_0$ ) and local structure environment around the absorbing atoms, including CN, bond distance, and the Debye-Waller factor, were allowed to vary during the fitting process.

**2.3. Electrochemical Measurements.** To prepare a catalyst-coated working electrode, 5 mg of the catalyst was ultrasonically dispersed in a mixture of deionized water (0.25 mL), ethanol (0.25 mL), and Nafion solution (5%, 25  $\mu\text{L}$ ) for 1 h to form a uniform catalyst ink. A total of 2  $\mu\text{L}$  of well-dispersed catalyst ink was pipetted and spread onto the prepolished GC electrode ( $d = 3 \text{ mm}$ ) and dried in air for 1 h before measurements. All electrochemical experiments were evaluated on a CHI 750D electrochemical workstation at room temperature (25 °C) using a standard three-electrode electrochemical cell. The cell consists of a glassy carbon working electrode (GC electrode, 3 mm inner diameter), an Ag/AgCl (3 M KCl) reference electrode, and a platinum foil counter electrode. All potentials were referenced to a reversible hydrogen electrode (RHE) by adding a value of  $(0.209 + 0.059 \times \text{pH}) \text{ V}$ . The scan was pretreated for 30 cycles between  $-0.2$  and  $1.0 \text{ V}$  at a sweep rate of  $100 \text{ mV}\cdot\text{s}^{-1}$  to remove any surface contamination prior to the MOR activity test. To determine the electrochemically active surface area (ECSA), the cyclic voltammetry (CV) experiments were conducted in N<sub>2</sub>-saturated 0.5 M H<sub>2</sub>SO<sub>4</sub> solution by potential cycling between  $-0.2$  and  $1.00 \text{ V}$  with a scan rate of  $50 \text{ mV}\cdot\text{s}^{-1}$ . The ECSA of the catalyst was calculated by the hydrogen under potential desorption ( $H_{\text{upd}}$ ) area after double-layer correction of the catalyst. The CV for MOR in an acidic medium was recorded in a N<sub>2</sub>-saturated solution containing 0.5 M H<sub>2</sub>SO<sub>4</sub> and 1.0 M CH<sub>3</sub>OH from  $-0.2$  to  $1.0 \text{ V}$  at a scan rate of  $50 \text{ mV}\cdot\text{s}^{-1}$ . The CV for MOR in alkaline medium was recorded in N<sub>2</sub>-saturated solution containing 0.1 M KOH and 1 M CH<sub>3</sub>OH from  $-0.9$  to  $0.2 \text{ V}$  at a scan rate of  $50 \text{ mV}\cdot\text{s}^{-1}$ . Amperometric current density-time ( $i-t$ ) curves were measured for 3000 s in N<sub>2</sub>-saturated solution containing 0.5 M H<sub>2</sub>SO<sub>4</sub> and 1.0 M CH<sub>3</sub>OH at 0.93 V vs RHE or N<sub>2</sub>-saturated solution containing 0.1 M KOH and 1.0 M CH<sub>3</sub>OH at 0.90 V vs RHE. Linear sweep voltammograms (LSV) were acquired in an O<sub>2</sub>-saturated 0.1 M KOH or 0.1 M HClO<sub>4</sub> aqueous solution at various rotation rates (400–2400 rpm). Before each measurement, the electrolyte was bubbled with O<sub>2</sub> for 30 min. A flow of O<sub>2</sub> was maintained over the electrolyte during the measurement to ensure a continuous O<sub>2</sub> saturation. Electrochemical impedance spectroscopy (EIS) of different catalysts was measured in the dark using a Zennium electrochemical workstation (Zahner, Germany) in a three-electrode system with an Ag/AgCl (3 M KCl) electrode as the reference, Pt as the counter electrode, and different solutions as the electrolyte (1.0 M CH<sub>3</sub>OH + 0.5 M H<sub>2</sub>SO<sub>4</sub>, 1.0 M CH<sub>3</sub>OH + 0.1 M KOH, O<sub>2</sub>-saturated 0.1 M HClO<sub>4</sub>, and O<sub>2</sub>-saturated 0.1 M KOH solutions) with the frequency ranging from 100 mHz to 10 kHz and a potential amplitude of 10 mV at different bias potentials vs RHE.

## 3. RESULTS AND DISCUSSION

**Construction of 2D Layered Mesoporous Mono- and Binary-TMN/G Catalysts.** To construct 2D layered mesoporous mono- and binary-TMN/G catalysts, a 2D layered mesoporous KIT-6/G template was specially designed. As seen

Scheme 1. Schematic Illustration of the Process Adopted for Synthesis of 2D Layered Mesoporous Pt/TMN/G Catalysts



in Scheme 1, the KIT-6/G template was created by in situ assembly of KIT-6 on the surface of free-standing GO nanosheets to form KIT-6/GO and then calcined in air and nitrogen atmospheres to remove pore former and convert GO to graphene. With such a 2D layered mesoporous KIT-6/G template, the mesoporous voids of KIT-6 could be available spaces to form size-controlled TMN nanoparticles. Meanwhile, the mesoporous structure of KIT-6 can be duplicated after its removal. Furthermore, as graphene was initially composited with KIT-6, the follow-up composition process of TMN with graphene was avoided, resulting in the compact integration of TMN with graphene. In detail, the synthetic process of Pt/TMN/G catalysts involves four steps, as described below: First, mesoporous KIT-6 was assembled in situ on the surface of GO nanosheets to form a 2D layered KIT-6/GO using ethyl silicate as the silicon source and P123 as the soft template. Further, the calcination treatment was carried out to remove P123 and transform the GO to graphene. Then, common transition-metal salts were infiltrated into the pore channels of the KIT-6/G template via a wet-impregnation method. The resulting nanocomposites were further annealed to decompose transition-metal salts into transition-metal oxide/graphene nanocomposites. Through the removal of the KIT-6 template via alkaline etching and nitridation treatment under  $\text{NH}_3$  atmosphere at a high temperature, 2D layered mesoporous mono- and binary-TMN/G were obtained. Finally, Pt nanoparticles were deposited on TMN/G nanocomposites via a polyol reduction route to achieve 2D layered mesoporous Pt/TMN/G catalysts. The synthetic strategy is quite robust and universal for synthesis of 2D layered mesoporous TMN nanocomposites, as demonstrated in our study for the synthesis of mono-Pt/TiN/G, Pt/CrN/G, Pt/WN/G, and Pt/Mo<sub>2</sub>N/G and binary-Pt/Ti<sub>0.5</sub>Cr<sub>0.5</sub>N/G, Pt/Ti<sub>0.8</sub>W<sub>0.2</sub>N/G, and Pt/Ti<sub>0.8</sub>Mo<sub>0.2</sub>N/G with large surface areas and very small TMN nanoparticles. The regularity of 2D layered mesoporous Pt/TMN/G catalysts is largely dependent on the quality of the KIT-6/G template.

**Phase Structure, Morphology, Size, and 2D Configuration.** SEM images reveal that the KIT-6/G template possesses randomly aggregated and crumpled layer-shaped structures closely packed with each other, which is similar to that of graphene flakes (Figures S1a and b). The formation of the 2D layered structure of the KIT-6/G template indicates that KIT-6 was successfully assembled onto the surface of free-standing graphene nanosheets.<sup>39</sup> TEM results further verify that

the KIT-6/G template exhibits very thin 2D flake morphology (Figures 1a–c and Figures S1c and d) because the whole area of graphene is nearly transparent under an electron beam (Figure 1a). Furthermore, it is observed that the KIT-6/G template has abundant pore channels distributed along the [110] and [100] directions (Figures S1c and d). High-magnification TEM characterization clearly displays the presence of pore channels with sizes of  $\sim 8$  nm (Figures 1b and c). The low-angle X-ray diffraction pattern of the KIT-6/G template displays two diffraction peaks corresponding to the (211) and (332) lattice planes, further confirming the formation of an ordered mesoporous structure (Figure 1d).

The crystallographic phase structure of TMN/G nanocomposites and Pt/TMN/G catalysts was studied using the XRD technique. The XRD patterns of 2D layered mesoporous TiN/G, Ti<sub>0.5</sub>Cr<sub>0.5</sub>N/G, and CrN/G nanocomposites and Pt/TiN/G, Pt/Ti<sub>0.5</sub>Cr<sub>0.5</sub>N/G, and Pt/CrN/G are shown in Figure 1e. Three strong diffraction peaks centered at 36.6°, 42.6°, and 61.8° in TiN/G, corresponding to the (111), (200), and (220) lattice planes of TiN, are observed, suggesting the formation of face centered cubic (FCC) TiN (JCPDS #38-1420).<sup>32,36</sup> The XRD pattern of CrN/G can be indexed well with the expected FCC CrN (JCPDS #65-9001).<sup>40</sup> The diffraction peaks at 36.2°, 42.2°, 61.3°, 73.4°, and 77.3° can be assigned to the (111), (200), (220), (311), and (222) lattice planes of FCC Ti<sub>0.5</sub>Cr<sub>0.5</sub>N (JCPDS #04-016–6620).<sup>36,38</sup> The diffraction peaks are similar to those of TiN/G and CrN/G and are located between the diffraction peaks of TiN/G and CrN/G, indicating the formation of Ti<sub>0.5</sub>Cr<sub>0.5</sub>N solid solution. Only a weak broad peak can be observed at  $\sim 26.2^\circ$ , belonging to the (002) lattice plane of graphene in all XRD patterns, indicating the presence of a small amount of graphene in TMN/G.<sup>31</sup> The average size of TiN, Ti<sub>0.5</sub>Cr<sub>0.5</sub>N, and CrN crystallites in TiN/G, Ti<sub>0.5</sub>Cr<sub>0.5</sub>N/G, and CrN/G are estimated to be 8.3, 6.4, and 12.1 nm, respectively, according to the Scherrer formula based on the diffraction peak of the (200) crystal plane. The smallest size of Ti<sub>0.5</sub>Cr<sub>0.5</sub>N nanocrystals indicates that the compositing of TiN and CrN crystals is beneficial for refining the grain size, which is consistent with the previous report.<sup>36</sup> The small size of Ti<sub>0.5</sub>Cr<sub>0.5</sub>N nanocrystals is in favor of the intimate contact of Pt with Ti<sub>0.5</sub>Cr<sub>0.5</sub>N, which should be largely favorable for promoting their “synergistic effect” for highly effective electrocatalysis.<sup>29</sup> After loading Pt nanoparticles onto TMN/G, three new broad peaks assigned to cubic phase of Pt (JCPDS #04-0802) appeared at 39.8, 46.2, and 67.5°, respectively, which

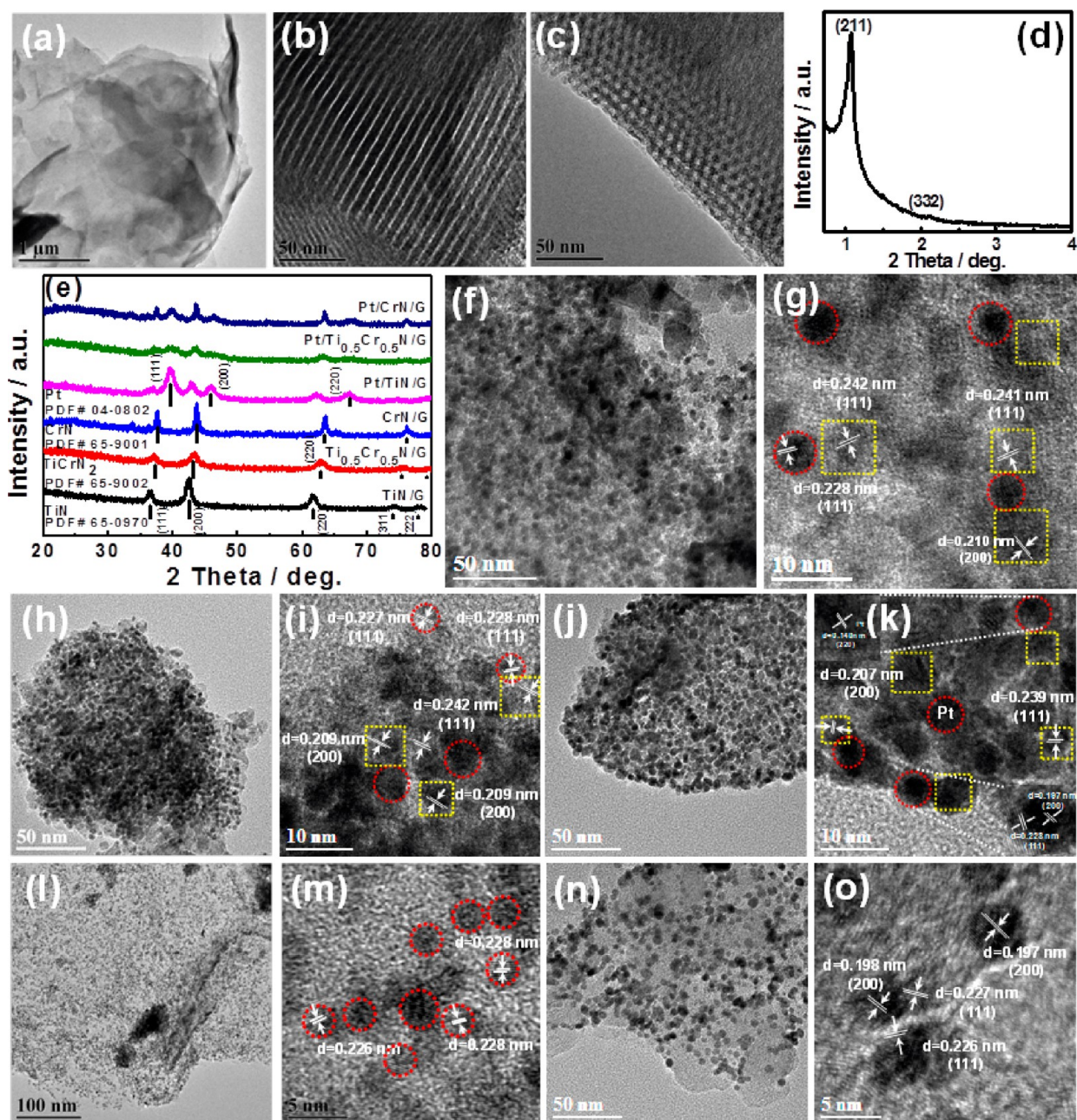


**Figure 1.** (a–c) TEM images of KIT-6/G nanocomposites under different magnifications. (d) Low-angle X-ray diffraction pattern of KIT-6/G nanocomposite. (e) XRD patterns of TiN/G,  $\text{Ti}_{0.5}\text{Cr}_{0.5}\text{N}/\text{G}$ , and CrN/G nanocomposites and Pt/TiN/G, Pt/ $\text{Ti}_{0.5}\text{Cr}_{0.5}\text{N}/\text{G}$ , and (f) Pt/CrN/G catalysts. TEM images of (f) Pt/TiN/G, (h) Pt/ $\text{Ti}_{0.5}\text{Cr}_{0.5}\text{N}/\text{G}$ , (j) Pt/CrN/G, (l) Pt/G, and (n) Pt/C catalysts and HRTEM images of (g) Pt/TiN/G, (i) Pt/ $\text{Ti}_{0.5}\text{Cr}_{0.5}\text{N}/\text{G}$ , (k) Pt/CrN/G, (m) Pt/G, and (o) Pt/C catalysts.

indicates that Pt/TMN/G was successfully obtained. The size of Pt nanoparticles is calculated to be  $\sim 4$  nm according to the Scherrer formula based on the diffraction peak of the (111) crystal plane. The presence of a small amount of Pt nanoparticles may be caused by the confined effect of mesopores existing in TMN/G, which is beneficial for exposing more active sites and improving the electrocatalytic performance.

The XRD patterns of GO, Pt/G, and Pt/C are shown in Figure S2. The strong peak centered at  $9.8^\circ$  belongs to the (002) crystal plane of GO, while the three strong peaks are typically attributed to the cubic phase of Pt, and the hump centered at  $25.4^\circ$  is assigned to the (002) lattice plane of

graphite carbon for Pt/G and Pt/C. The results indicate that high-quality GO, Pt/G, and Pt/C were successfully achieved. The phase structure of other mesoporous mono- and binary-TMN/G and their corresponding mono- and binary-Pt/TMN/G after Pt nanoparticles were loaded were also characterized by the XRD technique, as shown in Figures S3 and S4. The results reveal that mesoporous  $\text{Mo}_2\text{N}/\text{G}$ ,  $\text{WN}/\text{G}$ , Pt/ $\text{WN}/\text{G}$ , Pt/ $\text{Mo}_2\text{N}/\text{G}$ ,  $\text{Ti}_{0.8}\text{Mo}_{0.2}\text{N}/\text{G}$ ,  $\text{Ti}_{0.8}\text{W}_{0.2}\text{N}/\text{G}$ , Pt/ $\text{Ti}_{0.8}\text{Mo}_{0.2}\text{N}/\text{G}$ , and Pt/ $\text{Ti}_{0.8}\text{W}_{0.2}\text{N}/\text{G}$  can also be successfully prepared. The diffraction peaks of  $\text{Ti}_{0.8}\text{Mo}_{0.2}\text{N}/\text{G}$ ,  $\text{Ti}_{0.8}\text{W}_{0.2}\text{N}/\text{G}$ , Pt/ $\text{Ti}_{0.8}\text{Mo}_{0.2}\text{N}/\text{G}$ , and Pt/ $\text{Ti}_{0.8}\text{W}_{0.2}\text{N}/\text{G}$  are almost identical to those of TiN and are slightly shifted to a higher angle,

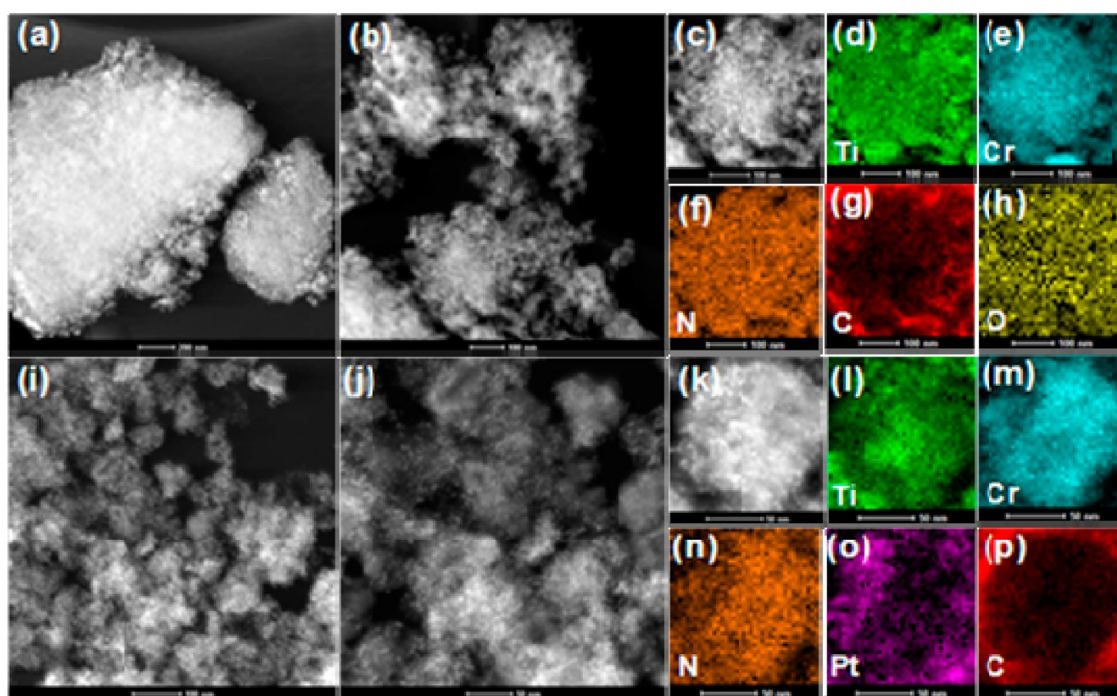


**Figure 2.** HAADF-STEM images of (a–c) the  $\text{Ti}_{0.5}\text{Cr}_{0.5}\text{N}/\text{G}$  nanocomposite and (i–k)  $\text{Pt}/\text{Ti}_{0.5}\text{Cr}_{0.5}\text{N}/\text{G}$  catalyst. Elemental mapping of (d) Ti, (e) Cr, (f) N, (g) C, and (h) O in the  $\text{Ti}_{0.5}\text{Cr}_{0.5}\text{N}/\text{G}$  nanocomposite and (l) Ti, (m) Cr, (n) N, (o) Pt, and (p) C in the  $\text{Pt}/\text{Ti}_{0.5}\text{Cr}_{0.5}\text{N}/\text{G}$  catalyst.

suggesting that Mo and W are incorporated into FCC-structured TiN to form a single-phase solution.<sup>35</sup>

TEM was used to characterize 2D layered mesoporous Pt/TiN/G, Pt/ $\text{Ti}_{0.5}\text{Cr}_{0.5}\text{N}/\text{G}$ , and Pt/CrN/G to identify their morphology, crystal size, microstructure, and pore structure. Figures 1f–k show the TEM and HRTEM images of Pt/TiN/G, Pt/ $\text{Ti}_{0.5}\text{Cr}_{0.5}\text{N}/\text{G}$ , and Pt/CrN/G. The low-magnification TEM images show that Pt/TiN/G, Pt/ $\text{Ti}_{0.5}\text{Cr}_{0.5}\text{N}/\text{G}$ , and Pt/CrN/G are composed of graphene, Pt, and TMN nanoparticles which are uniformly dispersed on graphene surface (Figures 1f, h, and j). The alternately dark and bright TEM images reveal that the stacking of TMN on the graphene surface forms mesoporous-structured Pt/TMN/G.<sup>41</sup> To verify the role of the KIT-6 template during the formation of the mesoporous structure, we also synthesized TiN/G by direct hydrolysis of the TOBT precursor on the graphene surface followed with nitridation treatment under a  $\text{NH}_3$  atmosphere. The TEM images show that there are no mesopores presented in the obtained TMN/G instead of the aggregation of large amounts of TiN nanoparticles on graphene surface (Figure S5). It can be clearly seen that the mesoporous structure in Pt/TMN/G is different from the mesoporous structure derived from the inverse replica of the three-dimensional (3D) KIT-6 template.<sup>42,43</sup> In our Pt/TMN/G, the mesopores are distributed along with the graphene nanosheets in 2D directions, whereas in the traditional mesoporous materials synthesized using KIT-6 as the hard template, the mesopores are present in 3D directions.<sup>42</sup> Meanwhile, replication for the pore channels in KIT-6 is incomplete in our Pt/TMN/G nanocomposites, and the TMN exist in granular rather than clubbed forms, generated from the perfect replicating of the pore channels in KIT-6. The results may be caused by the low-level filling fraction of precursors and the strong interaction of precursors with graphene. The TEM images also reveal that the size of uniformly distributed TiN,  $\text{Ti}_{0.5}\text{Cr}_{0.5}\text{N}$ , and CrN nanocrystals on the graphene surface is  $\sim 7$  nm, which is

smaller than that of pore channels of KIT-6 due to the shrinkage of TMN when experiencing the calcination process. The HRTEM images of Pt/TiN/G, Pt/ $\text{Ti}_{0.5}\text{Cr}_{0.5}\text{N}/\text{G}$ , and Pt/CrN/G nanocomposites reveal that all nanocomposites possess good crystallinity (Figures 1g, i, and k). For Pt/TiN/G nanocomposites, the good crystallinity of TiN marked by the yellow broken circle and Pt marked by the red broken square is clearly observed from the well-defined crystalline lattices with a lattice spacing of 0.242, 0.210, and 0.228 nm, corresponding to the (111) and (200) crystal planes of FCC TiN and the (111) crystal plane of cubic-phase Pt (Figure 1g).<sup>31,35,37</sup> The HRTEM images of Pt/ $\text{Ti}_{0.5}\text{Cr}_{0.5}\text{N}/\text{G}$  and Pt/CrN/G nanocomposites are similar to those of Pt/TiN/G nanocomposites. For Pt/ $\text{Ti}_{0.5}\text{Cr}_{0.5}\text{N}/\text{G}$  nanocomposites, the crystalline interplanar spacings of 0.240, 0.209, and 0.227 nm correspond to the (111) and (200) crystal planes of the FCC  $\text{Ti}_{0.5}\text{Cr}_{0.5}\text{N}$  solid solution (marked by the yellow broken square) and the (111) crystal plane of cubic-phase Pt (marked by the red broken circle), respectively (Figure 1i). Similarly, the crystalline interplanar spacings of 0.239, 0.207, 0.228, and 0.187 nm correspond to the (111) and (200) crystal planes of FCC CrN (marked by the yellow broken square) and the (111) and (200) crystal planes of cubic-phase Pt (marked by the red broken circle), respectively (Figure 1j) in Pt/CrN/G nanocomposites. The crystalline interplanar spacings of the (111) and (200) crystal planes of  $\text{Ti}_{0.5}\text{Cr}_{0.5}\text{N}$  nanocrystals in Pt/ $\text{Ti}_{0.5}\text{Cr}_{0.5}\text{N}/\text{G}$  nanocomposites are situated between the interplanar spacings of (111) and (200) crystal planes of TiN and CrN, further indicating the formation of a  $\text{Ti}_{0.5}\text{Cr}_{0.5}\text{N}$  solid solution. This is in good agreement with the XRD results. The HRTEM results still indicate that the Pt nanoparticles ( $\sim 3$ – $5$  nm) are uniformly loaded onto the surface of TMN/G nanocomposites due to the overlap of lattice fringes belonging to TMN and Pt, which is conducive to an increase in the number of active sites and an enhancement of the synergistic effect between TMN and Pt.<sup>29</sup> As the control samples, Pt/G and Pt/C were also

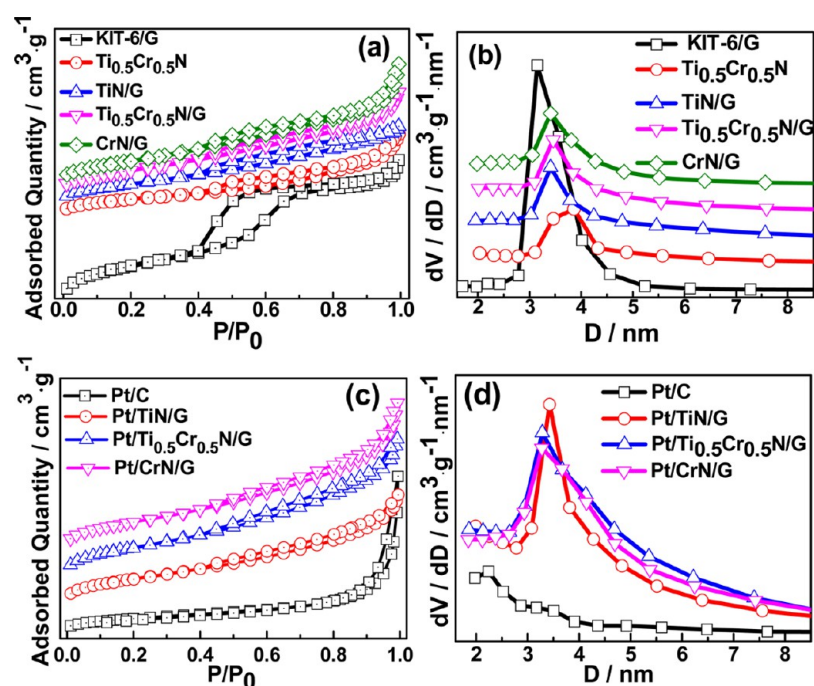


**Figure 3.** (a) N<sub>2</sub> adsorption–desorption isotherms and (b) pore size distribution of the KIT-6/G, Ti<sub>0.5</sub>Cr<sub>0.5</sub>N, TiN/G, Ti<sub>0.5</sub>Cr<sub>0.5</sub>N/G, and CrN/G nanocomposites. (c) N<sub>2</sub> adsorption–desorption isotherms and (d) pore size distribution of the Pt/C, Pt/TiN/G, Pt/Ti<sub>0.5</sub>Cr<sub>0.5</sub>N/G, and Pt/CrN/G catalysts.

characterized to determine their particle size and morphology. Figures 1l and m and Figures 1n and o show that uniform Pt nanoparticles with the particle size of ~3–4 nm were successfully supported on the surface of graphene nanosheets and irregular carbon, respectively.

In addition, the mesoporous TMN/G were further characterized by SEM to confirm their morphology and structure. Figures S6 and S7 display the SEM images of Pt/TiN/G, Pt/Ti<sub>0.5</sub>Cr<sub>0.5</sub>N/G, and Pt/CrN/G and Ti<sub>0.8</sub>Mo<sub>0.2</sub>N/G, Ti<sub>0.8</sub>W<sub>0.2</sub>/G, Mo<sub>2</sub>N/G, and WN/G nanocomposites under different magnifications. Obviously, all mesoporous TMN/G nanocomposites possess a stacked layered structure composed of small sizes of TMN nanocrystals. A large amount of TMN nanocrystals gather together and form numerous mesopores. The TEM images of 2D layered mesoporous TiN/G, Ti<sub>0.5</sub>Cr<sub>0.5</sub>N/G, and CrN/G nanocomposites are displayed in Figure S8. This further proves that the TMN/G are composed of uniform TMN nanocrystals dispersed on the graphene nanosheet surface, and the stacking of TMN nanocrystals forms a large amount of mesopores. Meanwhile, the TEM images of Ti<sub>0.8</sub>Mo<sub>0.2</sub>N/G, Ti<sub>0.8</sub>W<sub>0.2</sub>/G, Mo<sub>2</sub>N/G, and WN/G also display the existence of mesoporous structures (Figure S9). This further suggests that our synthesis method possesses universality.

High-angle annular dark field scanning transmission electron microscopy (HAADF-STEM) and elemental mapping were also performed to reveal the elemental distribution in 2D layered mesoporous Ti<sub>0.5</sub>Cr<sub>0.5</sub>N/G and Pt/Ti<sub>0.5</sub>Cr<sub>0.5</sub>N/G nanocomposites. The HAADF-STEM images in Figures 2a–c reveal that Ti<sub>0.5</sub>Cr<sub>0.5</sub>N/G is composed of small sizes of Ti<sub>0.5</sub>Cr<sub>0.5</sub>N nanoparticles. The structure is quite loose, and mesopores exist in the interparticles. Figures 2i–k show that Pt nanoparticles, observed as white dots, are remarkably well-dispersed on the surface of Pt/Ti<sub>0.5</sub>Cr<sub>0.5</sub>N/G nanocomposites, and no obvious aggregations are observed. The EDX elemental

mapping results shown in Figures 2d–h indicate that Ti, Cr, N, O, and C are spread evenly throughout the whole Ti<sub>0.5</sub>Cr<sub>0.5</sub>N/G nanocomposite, which shows the presence of Ti<sub>0.5</sub>Cr<sub>0.5</sub>N nanoparticles and graphene. The existence of O suggests that the surfaces of the Ti<sub>0.5</sub>Cr<sub>0.5</sub>N nanoparticles are slightly oxidized, which is in agreement with XPS results. After Pt nanoparticles were loaded on Ti<sub>0.5</sub>Cr<sub>0.5</sub>N/G nanocomposites, the EDX elemental mapping of Pt can be clearly seen in the obtained Pt/Ti<sub>0.5</sub>Cr<sub>0.5</sub>N/G nanocomposites, further indicating the successful support of Pt nanoparticles.

**Surface Area and Pore Property.** The nitrogen adsorption/desorption isotherms and the corresponding pore size distribution of KIT-6/G, Ti<sub>0.5</sub>Cr<sub>0.5</sub>N, TiN/G, Ti<sub>0.5</sub>Cr<sub>0.5</sub>N/G, and CrN/G are shown in Figures 3a and b. Figure 3a reveals that the KIT-6/G template exhibits a typical type IV isotherm with an H1 hysteresis loop, while the Ti<sub>0.5</sub>Cr<sub>0.5</sub>N and TMN (TiN, Ti<sub>0.5</sub>Cr<sub>0.5</sub>N and CrN)/G nanocomposites display a typical type IV isotherm with an H2 hysteresis loop. These results show that all TMN and TMN(TiN, Ti<sub>0.5</sub>Cr<sub>0.5</sub>N and CrN)/G possess mesopores, and the shape and structure of mesopores are different in template and mesoporous TMN/G nanocomposites generated via the inverse replication of the KIT-6/G template. The pore size distribution calculated from the desorption isotherms by the Barrett–Joyner–Halenda (BJH) method reveals that the pore size in the KIT-6/G template is distributed around 3.2 nm, while the pore sizes in Ti<sub>0.5</sub>Cr<sub>0.5</sub>N and TMN(TiN, Ti<sub>0.5</sub>Cr<sub>0.5</sub>N, and CrN)/G nanocomposites are larger than that in the KIT-6/G template, with the pore sizes distributed around 3.9, 3.5, 3.5, and 3.4 nm, respectively (Figure 3b and Table 1). Figures 3c and d show the nitrogen adsorption/desorption isotherms and the corresponding pore size distribution of Pt/TiN/G, Pt/Ti<sub>0.5</sub>Cr<sub>0.5</sub>N/G, and Pt/CrN/G, respectively. Pt/C exhibits a typical type II isotherm with a hysteresis loop at high relative pressure (P/P<sub>0</sub> > 0.85), indicating that Pt/C exists as a macropore instead of

**Table 1.** BET and BJH Properties of TMN/G Nanocomposites and Pt/TMN/G Catalysts

sample	$S_{\text{BET}}$ ( $\text{m}^2\cdot\text{g}^{-1}$ )	$V_p$ ( $\text{cm}^3\cdot\text{g}^{-1}$ ) <sup>a</sup>	$D_p$ (nm) <sup>b</sup>
KIT-6/G	329	0.45	3.2
Ti <sub>0.5</sub> Cr <sub>0.5</sub> N	138	0.22	3.9
TiN/G	211	0.31	3.5
Ti <sub>0.5</sub> Cr <sub>0.5</sub> N/G	216	0.36	3.5
CrN/G	201	0.33	3.4
Pt/TiN/G	171	0.27	3.4
Pt/Ti <sub>0.5</sub> Cr <sub>0.5</sub> N/G	190	0.33	3.2
Pt/CrN/G	180	0.30	3.2
Pt/C	100	0.37	

<sup>a</sup>BJH desorption cumulative volume of pores between 1.70 and 300.0 nm in diameter. <sup>b</sup>Calculated by the BJH method from the desorption isotherm linear plot.

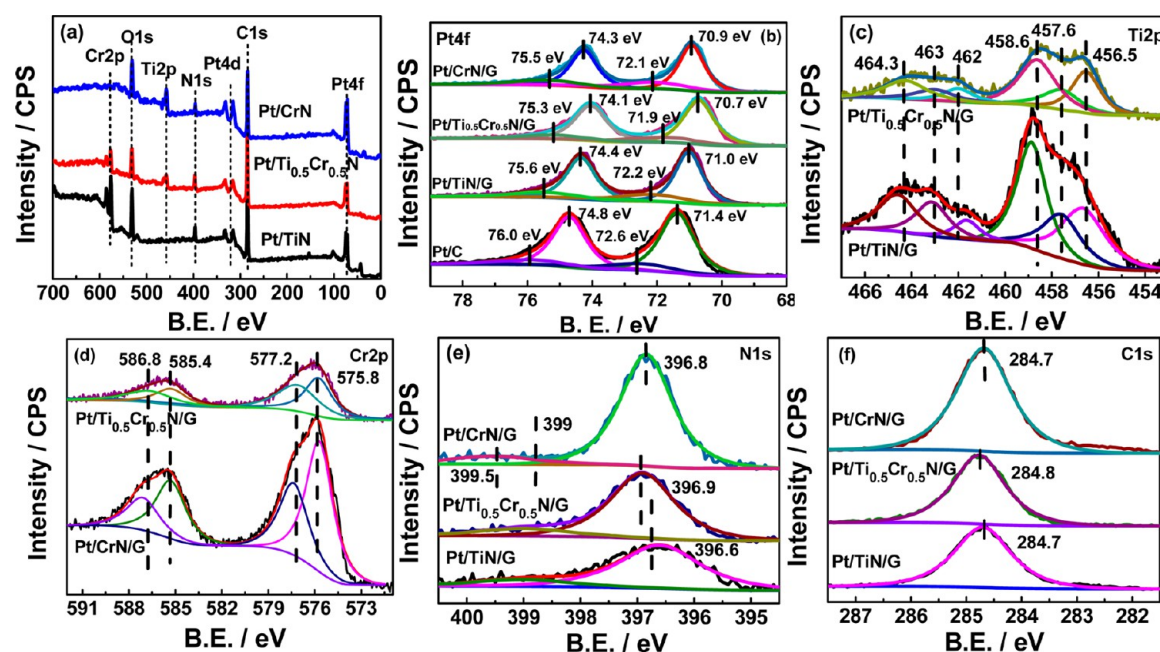
a mesopore derived from the stacking of Pt/C particles. The Pt/TMN/G (TMN = TiN, Ti<sub>0.5</sub>Cr<sub>0.5</sub>N, and CrN) nanocomposites present typical type IV isotherms with H2 hysteresis loops, which are identical to their corresponding TMN/G nanocomposites, indicating that after Pt nanoparticles were loaded onto TMN, the pore structure has no obvious alternation. The narrowing hysteresis loop suggests that Pt nanoparticles were successfully incorporated into the pore of the corresponding TMN/G nanocomposites. The smaller pore sizes in catalysts further confirm this point. High dispersion of Pt nanoparticles in mesopores may be beneficial for increasing the numbers of exposed active sites, inhibiting the agglomeration of Pt nanoparticles and enhancing the synergistic effect of Pt nanoparticles with TMN supports.

The BET surface area and pore volume of TMN/G and Pt/TMN/G are summarized in Table 1. As the template for construction of 2D layered TMN/G nanocomposites, KIT-6/G has a surface area of 329  $\text{m}^2\cdot\text{g}^{-1}$  with a pore volume of 0.45  $\text{cm}^3\cdot\text{g}^{-1}$ . Through the nanocasting method with KIT-6/G as the template, a series of TMN/G nanocomposites of TiN/G,

Ti<sub>0.5</sub>Cr<sub>0.5</sub>N/G, and CrN/G were successfully achieved and possess surface areas of 211, 216, and 201  $\text{m}^2\cdot\text{g}^{-1}$  with pore volumes of 0.31, 0.36, and 0.33  $\text{cm}^3\cdot\text{g}^{-1}$ , respectively, which show a decreasing trend both of surface area and pore volume. As expected, after Pt nanoparticles were loaded, the Pt/TiN/G, Pt/Ti<sub>0.5</sub>Cr<sub>0.5</sub>N/G, and Pt/CrN/G catalysts exhibit a slightly decreasing surface area and pore volume but still maintain over 170  $\text{m}^2\cdot\text{g}^{-1}$  of surface area, which is higher than the 100  $\text{m}^2\cdot\text{g}^{-1}$  surface area of Pt/C and other previously reported Pt/TMN or Pt/TMN/G catalysts.<sup>26,35</sup> Meanwhile the wider pore size distribution suggests that most of the Pt nanoparticles may be dispersed on the surface of TMN/G, whereas a small part of the Pt nanoparticles may be penetrated into the pores of TMN/G. The relatively high surface area of the present Pt/TMN/G catalysts may arise from their 2D layered mesoporous structure and result in outstanding catalytic activity due to the abundance of exposed active centers.

The N<sub>2</sub> adsorption–desorption isotherms and pore size distribution of the Pt/Ti<sub>0.8</sub>Mo<sub>0.2</sub>N and Pt/Ti<sub>0.8</sub>W<sub>0.2</sub>N catalysts were also tested. Figure S10a clearly exhibits that these samples display a typical type IV isotherm with an H2 hysteresis loop. It can also be confirmed by their pore size distribution, as shown in Figure S10b, which was distributed around 3.5 nm. These results further verify the universality of our synthesis method.

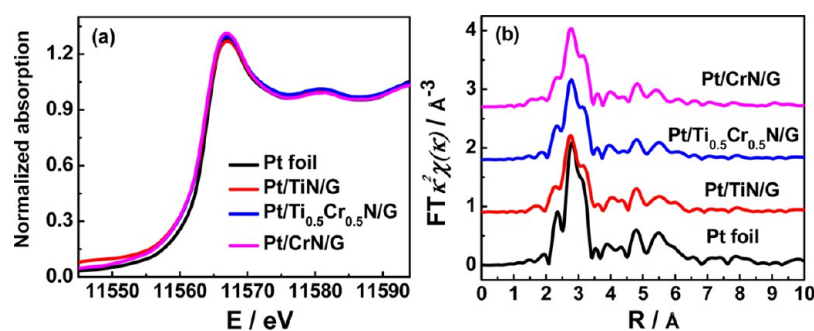
**Surface Chemical Composition and Elemental Valence State.** The surface chemical state of Pt/TMN/G (TM = TiN, Ti<sub>0.5</sub>Cr<sub>0.5</sub>N, and CrN) catalysts were probed using XPS. Figure 4 gives the full XPS and high-resolution XPS spectra for Pt 4f, Ti 2p, Cr 2p, N 1s, and C 1s of the Pt/TMN/G and Pt/C catalysts. It can be found from Figure 4a that the characteristic peaks of Pt 4f, Ti 2p, Cr 2p, N 1s, C 1s, and O 1s appeared at the binding energies of 72.0, 458.5, 577.0, 397.4, 284.7, and 531.8, indicating the presence of Pt, Ti, Cr, N, C, and O in the catalysts. According to the XPS spectra for Pt 4f of the Pt/TiN/G, Pt/Ti<sub>0.5</sub>Cr<sub>0.5</sub>N/G, Pt/CrN/G, and Pt/C catalysts shown in Figure 4b, each XPS profile of the Pt 4f region can be



**Figure 4.** (a) XPS survey spectra of Pt/TiN/G, Pt/Ti<sub>0.5</sub>Cr<sub>0.5</sub>N/G, and Pt/CrN/G catalysts and high-resolution XPS spectra for (b) Pt 4f, (c) Ti 2p, (d) Cr 2p, (e) N 1s, and (f) C 1s in Pt/TiN/G, Pt/Ti<sub>0.5</sub>Cr<sub>0.5</sub>N/G, Pt/CrN/G, and Pt/C catalysts.

**Table 2.** XPS Data for Evaluation of the Valence States of Pt, Ti, Cr, and N and the Content of N and Pt on the Surface of TMN/G Nanocomposites and Pt/TMN/G Catalysts

catalyst	Pt 4f7/2 (eV)	Ti 2p3/2 (eV)	Cr 2p3/2 (eV)	N 1s (eV)	metal (N)	pyridineN (at. %)	Pt <sup>0</sup> /Pt (%)
TiN/G		Ti–N 455.6		Ti–N 396.7			
		Ti–O–N 456.9		pyridineN 399.2	0.85	4.3	
		Ti–O 458.4					
Ti <sub>0.5</sub> Cr <sub>0.5</sub> N/G		Ti–N 456	Cr–N 575.5	Cr/Ti–N 396.9			
		Ti–O–N 457.4	Cr–O–N 577	pyridineN 399.4	1.23	3.3	
		Ti–O 458.5					
CrN/G			Cr–N 575.5	Cr–N 396.7			
			Cr–O–N 577.1	pyridineN 399.3	0.75	2.5	
Pt/TiN/G	Pt(0) 71.0	Ti–N 456.5		Ti–N 396.6			
	Pt(II) 72.2	Ti–O–N 457.6		pyridineN 399.0	0.99	3.5	75.2
		Ti–O 458.9					
Pt/Ti <sub>0.5</sub> Cr <sub>0.5</sub> N/G	Pt(0) 70.7	Ti–N 456.6	Cr–N 575.4	Cr/Ti–N 396.9			
	Pt(II) 71.9	Ti–O–N 457.6	Cr–O–N 576.9	pyridineN 399.0	0.96	2.8	76.4
		Ti–O 458.6					
Pt/CrN/G	Pt(0) 70.9		Cr–N 575.7	Cr–N 396.8			
	Pt(II) 72.1		Cr–O–N 577.3	pyridineN 399.6	1.06	2.2	74.4
Pt/C	Pt(0) 71.4						72.8
	Pt(II) 72.6						

**Figure 5.** (a) XANES spectra at the Pt L<sub>3</sub> edge of the Pt foil, Pt/TiN/G, Pt/Ti<sub>0.5</sub>Cr<sub>0.5</sub>N/G, and Pt/CrN/G catalysts and (b) *k*<sup>2</sup>-weighted Fourier transformed Pt L<sub>3</sub> edge EXAFS spectra (*R* space) of the Pt foil, Pt/TiN/G, Pt/Ti<sub>0.5</sub>Cr<sub>0.5</sub>N/G, and Pt/CrN/G catalysts.

deconvoluted into two pairs of doublet peaks. The peaks at 70.7—71.4 and 74.1—74.8 eV belong to metallic Pt(0), and the peaks at 71.9—72.6 and 75.3—76.0 eV are assigned to Pt(II).<sup>44–47</sup> Obviously, a negative shift occurs in XPS spectra of Pt 4f in the Pt/Ti<sub>0.5</sub>Cr<sub>0.5</sub>N/G catalyst. This suggests that there is an enhanced interaction between Pt nanoparticles and Ti<sub>0.5</sub>Cr<sub>0.5</sub>N supports compared to that between Pt nanoparticles and TiN or CrN supports.<sup>48,49</sup> The data summarized in Table 2 shows that the binding energy of Pt 4f in all Pt/TMN/G catalysts is lower than that of Pt 4f in the Pt/C catalyst, indicating the interaction existed in Pt nanoparticles, and TMN/G support is stronger than that existing in Pt nanoparticles and carbon supports. A negative shift of binding energy means that the increased electron density of Pt in the Pt/TMN/G catalysts, resulting from the electrons flowing from TMN to Pt, is a factor in the enhancement of catalytic activity.<sup>48,49</sup> A larger negative shift occurs in XPS spectra of Pt 4f in the Pt/Ti<sub>0.5</sub>Cr<sub>0.5</sub>N/G catalyst, suggesting that a stronger interaction existed in Pt nanoparticles and Ti<sub>0.5</sub>Cr<sub>0.5</sub>N/G supports. Moreover, the content of Pt(0) and Pt(II) in different electrocatalysts is distinct. The relative content of Pt(0) in the Pt/Ti<sub>0.5</sub>Cr<sub>0.5</sub>N/G catalyst (76.4 at. %) is slightly higher than that of Pt(0) in the Pt/TiN/G (75.2 at. %) and Pt/CrN/G (74.4 at. %) catalysts. More Pt(0) is conducive

to enhancing catalytic activity.<sup>35</sup> The high-resolution XPS spectra of N 1s, Ti 2p, and Cr 2p are well-fitted to several different related peaks. The N 1s peak can be fitted to two components based on different binding energies,<sup>33</sup> which can be assigned to pyridine-like N (399–399.4 eV) and essential nitride (396.6–396.8) (Figure 4c).<sup>50</sup> The contents of pyridine-like N in Pt/TiN/G, Pt/Ti<sub>0.5</sub>Cr<sub>0.5</sub>N/G, and Pt/CrN/G electrocatalysts are calculated to be 3.5, 2.8, and 2.2 at. %, respectively. This result implies that the graphene in catalysts is doped with N atoms.<sup>51</sup> Meanwhile, the position of the peak belonging to N 1s is slightly different due to the distinguishing interaction between transition metals and N. This may influence their electrocatalytic performance. The XPS spectra of Ti 2p can be deconvoluted into three couples of peaks (Figure 4d). The first couple of peaks at the position of low binding energy are assigned to TiN. The second couple of peaks at the middle binding energy correspond to oxynitride due to the partial oxidization of TiN. The third couple of peaks belong to the typical characteristics of Ti–O in TiO<sub>2</sub>.<sup>51,52</sup> These results imply that the surfaces of Pt/TiN/G and Pt/Ti<sub>0.5</sub>Cr<sub>0.5</sub>N/G catalysts are composed of TiN, oxynitride, and TiO<sub>2</sub> due to the formation of a very thin surface oxide layer upon their exposure to air.<sup>36</sup> From the XPS profile of Cr 2p, two peaks at the positions of 575.8 and 577.4 eV are identified.

Table 3. EXAFS Fitting Results of Pt/TMN/G Catalysts<sup>a</sup>

sample	Pt–Pt		DWF	$\Delta E_0$ (eV)	particle size
	R ( $\text{\AA}$ )	CN			
Pt foil	2.766 $\pm$ 0.002	12	0.0047 $\pm$ 0.0002	8.7 $\pm$ 0.4	
Pt/CrN/G	2.755 $\pm$ 0.006	9.2 $\pm$ 0.9			3.2
Pt/TiN/G	2.754 $\pm$ 0.003	8.8 $\pm$ 0.6	0.0057 $\pm$ 0.0004	9.4 $\pm$ 0.4	2.9
Pt/Ti <sub>0.5</sub> Cr <sub>0.5</sub> N/G	2.757 $\pm$ 0.004	9.4 $\pm$ 0.7			3.3

<sup>a</sup>R: distance; CN: coordination number; DWF: Debye–Waller factor.

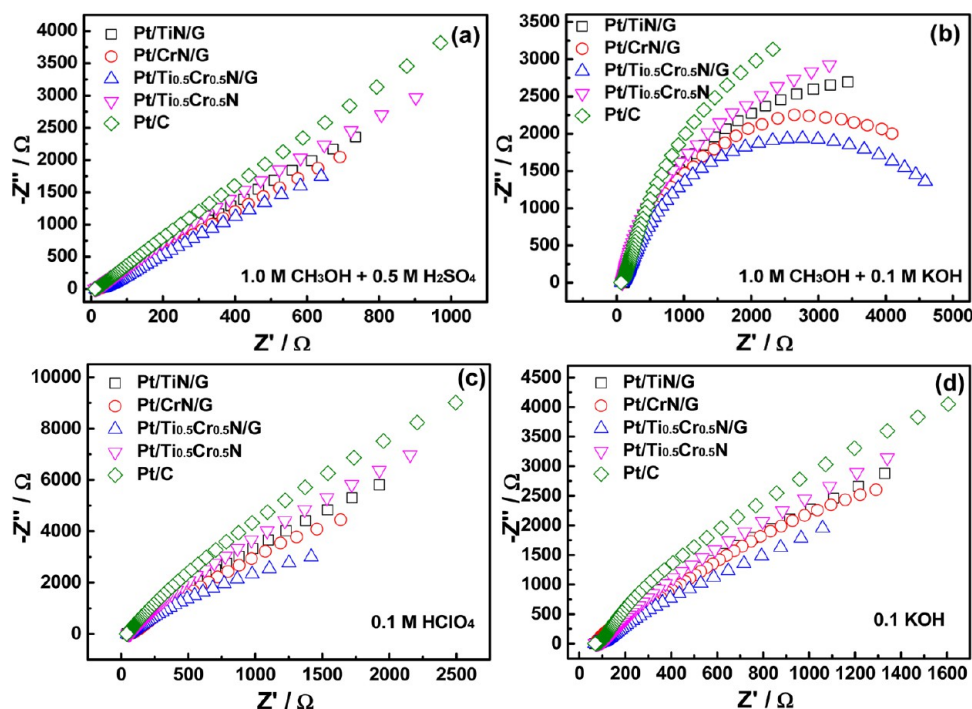


**Figure 6.** Nyquist plots of Pt/TiN/G, Pt/CrN/G, Pt/Ti<sub>0.5</sub>Cr<sub>0.5</sub>N/G, Pt/Ti<sub>0.5</sub>Cr<sub>0.5</sub>N, and Pt/C catalysts at different bias voltages versus RHE in different media: (a) 0.9 V in 1.0 M CH<sub>3</sub>OH + 0.5 M H<sub>2</sub>SO<sub>4</sub>, (b) 1.1 V in 1.0 M CH<sub>3</sub>OH + 0.1 M KOH, (c) 0.3 V in O<sub>2</sub>-saturated 0.1 M HClO<sub>4</sub>, and (d) 0.3 V in O<sub>2</sub>-saturated 0.1 M KOH.

The first one belongs to CrN (575.8 eV), and the latter one falls into the region of CrO<sub>x</sub> (576.3–576.8 eV) (Figure 4e).<sup>53</sup> This also indicates the formation of a thin CrO<sub>x</sub> layer on the surface of Pt/CrN/G and Pt/Ti<sub>0.5</sub>Cr<sub>0.5</sub>N/G catalysts. The C 1s XPS spectra show that the carbons existing in all catalysts have sp<sup>2</sup> hybridization, suggesting that the carbon comes from graphite carbon generated by the stack of graphene (Figure 4f). The presence of graphite carbon is helpful for the transfer of electrons in Pt/TMN/G catalysts. The XPS spectra of mesoporous TMN/G nanocomposites are shown in Figure S11. It is revealed that the XPS spectra of TMN/G nanocomposites are similar to their corresponding Pt/TMN/G catalysts, suggesting that after Pt nanoparticles were loaded on the TMN/G nanocomposites, the surface element composition and the valence state of the catalysts have no obvious changes.

#### Electronic Structure and Coordination Environment.

The X-ray absorption near-edge structure (XANES) spectra from the Pt L3 edge is given to provide information on the unoccupied electron density of d states. Figure 5 displays Pt L3 edge XANES spectra of Pt in Pt foil, Pt/TiN/G, Pt/Ti<sub>0.5</sub>Cr<sub>0.5</sub>N/G, and Pt/CrN catalysts. The spectra obtained for all Pt/TMN/G catalysts resemble that of the Pt foil, indicating the presence of metallic Pt. The related EXAFS

spectra in the R spaces of Pt foil, Pt/TiN/G, Pt/Ti<sub>0.5</sub>Cr<sub>0.5</sub>N/G, and Pt/CrN catalysts display a strong contribution by the first shell of Pt–Pt at  $\sim$ 2.7  $\text{\AA}$ , and no contribution by the first shell of Pt–O can be found. An overall damping of the spectra is observed for all Pt/TMN/G catalysts compared the spectra of bulk Pt, which indicates reduced atomic coordination numbers and enhanced structural disorder in the present nanostructured catalysts resulting from the small sizes of nanoparticles.<sup>54</sup> The corresponding coordination numbers (CN) obtained by the EXAFS fittings via the Artemis software are 9.2, 8.8, and 9.4 for the Pt/TiN/G, Pt/Ti<sub>0.5</sub>Cr<sub>0.5</sub>N/G, and Pt/CrN catalysts, respectively, which indicates that the particles size of Pt is  $\sim$ 3 nm in all catalysts, as listed in Table 3.<sup>55</sup> This is consistent with the Pt nanoparticle sizes found in the HRTEM results.

**Electrochemical Impedance.** To further examine the electrode kinetics during the electrocatalytic reaction process of different catalysts toward ORR and MOR in acidic and alkaline media, the electrochemical impedance spectra (EIS) of the Pt/TiN/G, Pt/CrN/G, Pt/Ti<sub>0.5</sub>Cr<sub>0.5</sub>N/G, Pt/Ti<sub>0.5</sub>Cr<sub>0.5</sub>N, and Pt/C catalysts were studied in O<sub>2</sub>-saturated 0.1 M HClO<sub>4</sub> and 0.1 M KOH and in N<sub>2</sub>-saturated 1.0 M CH<sub>3</sub>OH + 0.5 M H<sub>2</sub>SO<sub>4</sub> and 1.0 M CH<sub>3</sub>OH + 0.1 M KOH<sup>56,57</sup> the results are shown in Nyquist plots in Figure 6. Generally speaking, the semicircle diameter reflects the value of charge-transfer resistance, and a

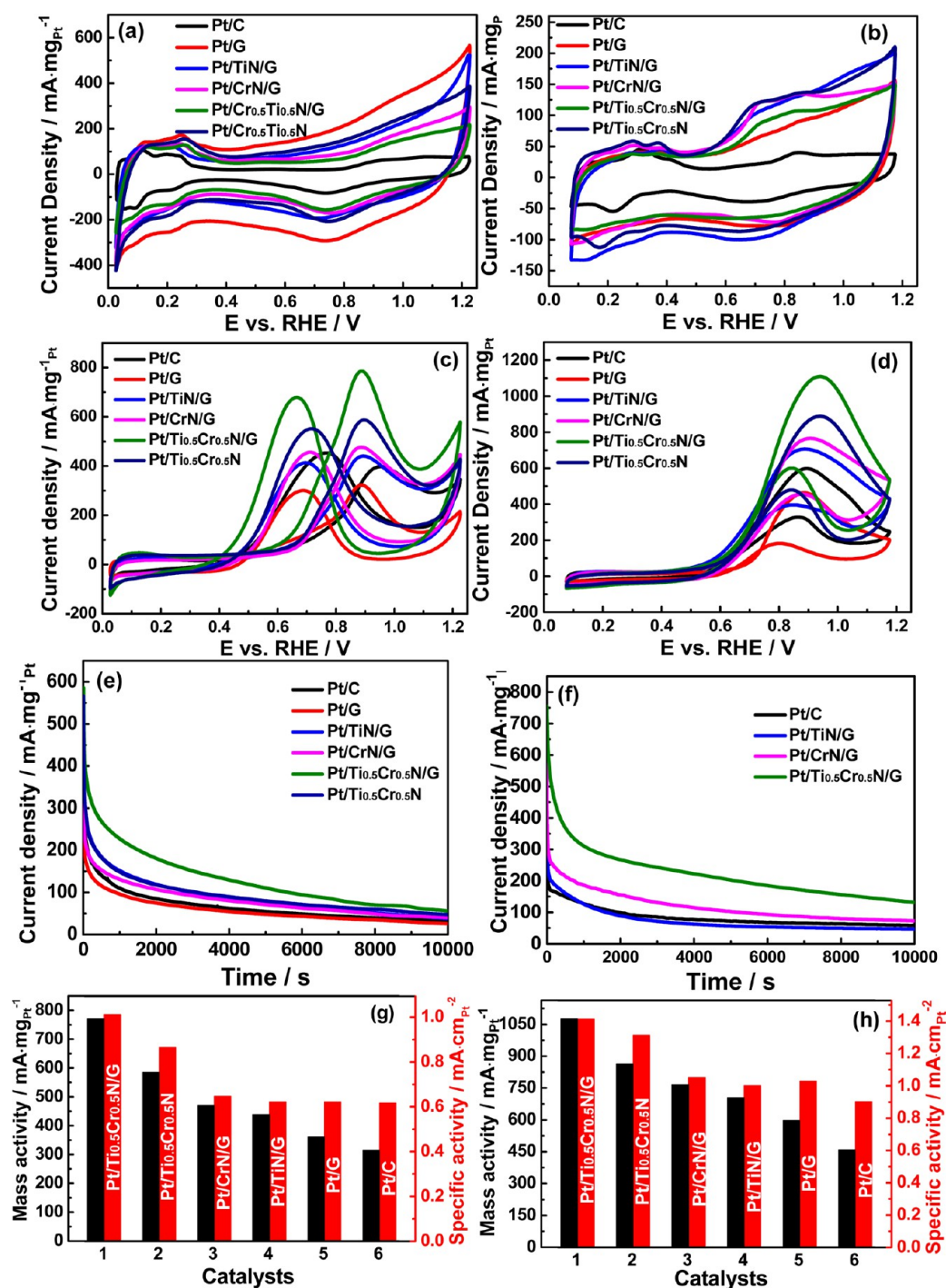


**Figure 7.** Cyclic voltammograms of the Pt/Ti<sub>0.5</sub>Cr<sub>0.5</sub>N/G, Pt/Ti<sub>0.5</sub>Cr<sub>0.5</sub>N, Pt/CrN/G, Pt/TiN/G, Pt/G, and Pt/C catalysts in (a) 0.5 M H<sub>2</sub>SO<sub>4</sub>, (b) 0.1 M KOH, (c) 1.0 M CH<sub>3</sub>OH + 0.5 M H<sub>2</sub>SO<sub>4</sub>, and (d) 1.0 M CH<sub>3</sub>OH + 0.1 M KOH. (e) Chronoamperometry curves of the Pt/Ti<sub>0.5</sub>Cr<sub>0.5</sub>N/G, Pt/Ti<sub>0.5</sub>Cr<sub>0.5</sub>N, Pt/CrN/G, Pt/TiN/G, Pt/G, and Pt/C catalysts in 1.0 M CH<sub>3</sub>OH + 0.5 M H<sub>2</sub>SO<sub>4</sub> at 0.93 V vs RHE. (f) Chronoamperometry curves of the Pt/Ti<sub>0.5</sub>Cr<sub>0.5</sub>N/G, Pt/CrN/G, Pt/TiN/G, and Pt/C catalysts in 1.0 M CH<sub>3</sub>OH + 0.1 M KOH at 0.9 V vs RHE (g and h) Mass- and area-specific activities of the Pt/Ti<sub>0.5</sub>Cr<sub>0.5</sub>N/G, Pt/Ti<sub>0.5</sub>Cr<sub>0.5</sub>N, Pt/CrN/G, Pt/TiN/G, Pt/G, and Pt/C catalysts for methanol oxidation at 0.9 V vs RHE in 1.0 M CH<sub>3</sub>OH + 0.5 M H<sub>2</sub>SO<sub>4</sub> and 1.0 M CH<sub>3</sub>OH + 0.1 M KOH. The scanning rate of the cyclic voltammograms was 100 mV s<sup>-1</sup> in 0.5 M H<sub>2</sub>SO<sub>4</sub> and 0.1 M KOH and 50 mV·s<sup>-1</sup> in 1.0 M CH<sub>3</sub>OH + 0.5 M H<sub>2</sub>SO<sub>4</sub> and 1.0 M CH<sub>3</sub>OH + 0.1 M KOH.

smaller diameter represents a lower charge-transfer resistance.<sup>58</sup> It can be clearly seen that the semicircles corresponding to the Pt/Ti<sub>0.5</sub>Cr<sub>0.5</sub>N/G catalysts possess the smallest diameter in both O<sub>2</sub>-saturated acidic and alkaline media and acidic and alkaline media containing methanol, implying that the Pt/Ti<sub>0.5</sub>Cr<sub>0.5</sub>N/G catalysts possess the lowest charge-transfer impedance, which indicates that the Pt/Ti<sub>0.5</sub>Cr<sub>0.5</sub>N/G catalysts

may possess the fastest electrocatalytic reaction kinetics.<sup>57,59–61</sup> The much larger semicircle of the graphene-free Pt/Ti<sub>0.5</sub>Cr<sub>0.5</sub>N catalyst suggests larger electron-transport resistance in the Pt/Ti<sub>0.5</sub>Cr<sub>0.5</sub>N sample in comparison with that in the Pt/TiN/G catalyst, suggesting that the addition of graphene can enhance the charge-transfer process in the catalyst during ORR and MOR. The Nyquist plots of the Pt/C catalyst are also provided

**Table 4.** Actual Pt Content in Various Catalysts for Methanol Electro-Oxidation and the Corresponding CV Parameters in Acidic Media<sup>a</sup>

catalyst	Pt (wt)	ECSA (m <sup>2</sup> ·g <sup>-1</sup> )	onset potential (V)	I <sub>f</sub> /I <sub>b</sub>	E <sub>p</sub> (V)	j <sub>p</sub> <sup>area</sup> (mA·cm <sup>-2</sup> )	j <sub>p</sub> <sup>mass</sup> (mA·mg <sub>Pt</sub> <sup>-1</sup> )
Pt/Ti <sub>0.5</sub> Cr <sub>0.5</sub> N <sub>2</sub> /G	15.6	76.2	0.46	1.16	0.89	1.04	785.4
Pt/Ti <sub>0.5</sub> Cr <sub>0.5</sub> N	14.8	65.7	0.47	1.07	0.90	0.89	395.8
Pt/CrN/G	15.2	72.8	0.48	1.05	0.89	0.65	587.2
Pt/TiN/G	14.9	70.5	0.51	1.09	0.90	0.62	476.8
Pt/G	19.8	50.9	0.47	1.07	0.89	0.63	322.4
Pt/C	15.5	58.1	0.46	0.88	0.94	0.68	440.2

<sup>a</sup>E<sub>p</sub>: peak potential; j<sub>p</sub><sup>area</sup>: area-normalized current densities; j<sub>p</sub><sup>mass</sup>: mass-normalized current densities; ECSA: electrochemically active surface area; I<sub>f</sub>/I<sub>b</sub>: ratio of forward oxidation current density to backward current density. All potentials were referenced to a reversible hydrogen electrode (RHE).

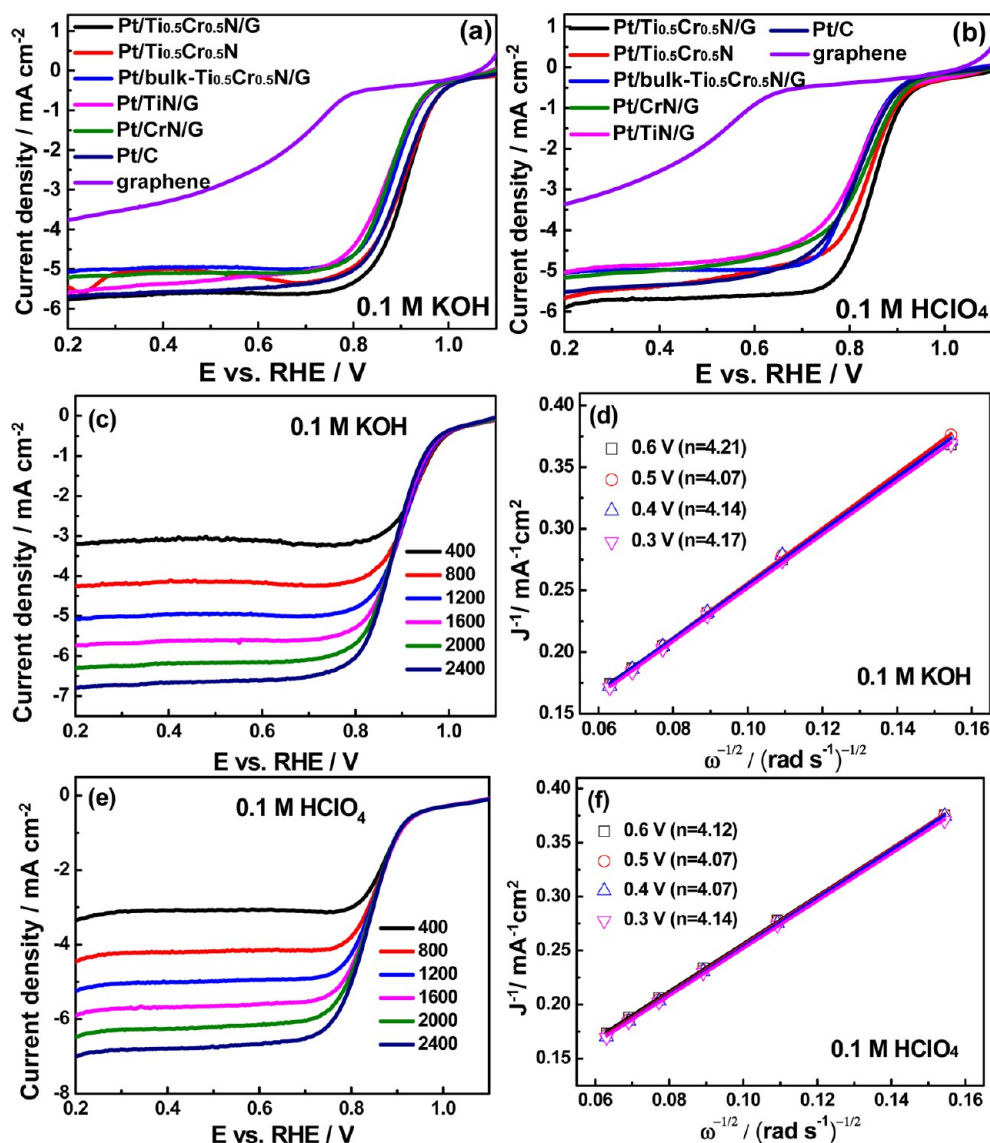


**Figure 8.** LSV curves of different catalysts at a rotation rate of 1600 rpm in O<sub>2</sub>-saturated (a) 0.1 M KOH and (b) 0.1 M HClO<sub>4</sub> media with a scan speed of 10 mV/s. (c) LSV curves of the Pt/Ti<sub>0.5</sub>Cr<sub>0.5</sub>N/G catalyst at rotation rates of 400–2400 rpm in 0.1 M KOH media. (d) Corresponding K–L plots at different potentials in 0.1 M KOH media. (e) LSV curves of the Pt/Ti<sub>0.5</sub>Cr<sub>0.5</sub>N/G catalyst at rotation rates of 400–2400 rpm in 0.1 M HClO<sub>4</sub> media. (f) Corresponding K–L plots at different potentials in 0.1 M HClO<sub>4</sub> media.

as comparison, and the largest semicircle diameter implies that the Pt/C catalyst exhibits a slower electron-transport property. Therefore, it can be predicted that the Pt/C catalyst may display an inferior electrocatalytic performance to those of the Pt/TiN/G and Pt/Ti<sub>0.5</sub>Cr<sub>0.5</sub>N catalysts.

**Electrocatalytic Performance.** Cyclic voltammetry (CV) was used to evaluate the comparative electrochemical catalytic performance of the Pt/C, Pt/G, Pt/Ti<sub>0.5</sub>Cr<sub>0.5</sub>N, Pt/TiN/G, Pt/Ti<sub>0.5</sub>Cr<sub>0.5</sub>N/G, and Pt/CrN/G catalysts. The electrochemical activity was evaluated and normalized with the Pt loading weight measured by ICP-MS and the electrochemical surface

area estimated from hydrogen adsorption–desorption charges. Figures 7a and b show CVs of different catalysts recorded at room temperature in  $N_2$ -purged 0.5 M  $H_2SO_4$  and 0.1 M KOH solutions at a scan rate of  $50 \text{ mV}\cdot\text{s}^{-1}$ . The ECSA ( $\text{m}^2\cdot\text{g}^{-1}_{\text{Pt}}$ ) for different catalysts were calculated using CV in an  $H_2SO_4$  solution (0.5 M) according to the equation  $\text{ECSA} = Q_{\text{H}} / (210 \times W_{\text{Pt}})$ , where  $W_{\text{Pt}}$  represents the Pt loading content ( $\text{mg}\cdot\text{cm}^{-2}$ ) on the electrode,  $Q_{\text{H}}$  is the total charge ( $\mu\text{C}$ ) for hydrogen desorption after double-layer correction, and 210 represents the charge ( $\mu\text{C}\cdot\text{cm}^{-2}_{\text{Pt}}$ ) required to oxidize a monolayer of hydrogen on a clean Pt surface.<sup>54</sup> The ECSA of the Pt/G, Pt/C, Pt/TiN/G, Pt/CrN/G, Pt/ $Ti_{0.5}Cr_{0.5}N$ , and Pt/ $Ti_{0.5}Cr_{0.5}N$ /G catalysts are 51.0, 58.1, 70.5, 72.8, 76.2, and 65.7  $\text{m}^2\cdot\text{g}^{-1}$ , respectively. The ECSA of the Pt/TMN/G catalyst is obviously higher than those of the Pt/G and Pt/C catalysts, suggesting that the presence of mesoporous structures in the Pt/TMN/G catalysts is beneficial for the dispersion of Pt nanoparticles and the exposure of active sites.<sup>52,54</sup> Among these catalysts, the Pt/ $Ti_{0.5}Cr_{0.5}N$ /G catalyst possess the highest ECSA, indicating that the small size of  $Ti_{0.5}Cr_{0.5}N$  nanocrystals is favorable for Pt nanoparticle dispersion.<sup>29</sup> Meanwhile, the existence of graphene is also conducive to improving the dispersibility of Pt nanoparticles.<sup>34</sup>

The electrocatalytic properties of the Pt/G, Pt/C, Pt/ $Ti_{0.5}Cr_{0.5}N$ , Pt/TiN/G, Pt/ $Ti_{0.5}Cr_{0.5}N$ /G, and Pt/CrN/G catalysts toward MOR were investigated in a 1.0 M  $CH_3OH$  + 0.5 M  $H_2SO_4$  and 1.0 M  $CH_3OH$  + 0.1 M KOH solutions. The best MOR activity was achieved in Pt/ $Ti_{0.5}Cr_{0.5}N$ /G with a Pt loading amount of  $\sim 20 \text{ wt } \%$  (Figure S12). Thus, the Pt content in all investigated catalysts was  $\sim 20 \text{ wt } \%$ . Figures 7c and d show that all Pt/TMN/G catalysts show higher catalytic activity than that of the Pt/C and Pt/G catalysts toward methanol electro-oxidation in the order of Pt/ $Ti_{0.5}Cr_{0.5}N$ /G > Pt/ $Ti_{0.5}Cr_{0.5}N$  > Pt/CrN/G > Pt/TiN/G > Pt/C > Pt/G. The Pt/ $Ti_{0.5}Cr_{0.5}N$ /G catalyst exhibits the highest catalytic activity for MOR in both acidic and alkaline media. The mass-normalized peak current density of the Pt/ $Ti_{0.5}Cr_{0.5}N$ /G catalyst in the positive direction is  $785.4 \text{ mA}\cdot\text{mg}^{-1}_{\text{Pt}}$  which is 1.34, 1.65, 1.78, 2.44, and 1.98 times higher than those of Pt/ $Ti_{0.5}Cr_{0.5}N$  ( $587.2 \text{ mA}\cdot\text{mg}^{-1}_{\text{Pt}}$ ), Pt/CrN/G ( $476.8 \text{ mA}\cdot\text{mg}^{-1}_{\text{Pt}}$ ), Pt/TiN/G ( $440.2 \text{ mA}\cdot\text{mg}^{-1}_{\text{Pt}}$ ), Pt/G ( $322.4 \text{ mA}\cdot\text{mg}^{-1}_{\text{Pt}}$ ), and Pt/C ( $395.8 \text{ mA}\cdot\text{mg}^{-1}_{\text{Pt}}$ ), respectively, in a 1.0 M  $CH_3OH$  + 0.1 M KOH solution (Figure 7e and Table 4). Meanwhile, in a 1.0 M  $CH_3OH$  + 0.1 M KOH solution, the Pt/ $Ti_{0.5}Cr_{0.5}N$ /G catalyst also displays the best MOR activity. The highest mass activity of the Pt/ $Ti_{0.5}Cr_{0.5}N$ /G catalyst in the positive direction can reach up to  $1068.8 \text{ mA}\cdot\text{mg}^{-1}_{\text{Pt}}$  which is 1.25, 1.51, 1.40, 2.31, and 1.79 times higher than that of Pt/ $Ti_{0.5}Cr_{0.5}N$  ( $856.4 \text{ mA}\cdot\text{mg}^{-1}_{\text{Pt}}$ ), Pt/CrN/G ( $764.1 \text{ mA}\cdot\text{mg}^{-1}_{\text{Pt}}$ ), Pt/TiN/G ( $706.2 \text{ mA}\cdot\text{mg}^{-1}_{\text{Pt}}$ ), Pt/G ( $461.8 \text{ mA}\cdot\text{mg}^{-1}_{\text{Pt}}$ ), and Pt/C ( $597.7 \text{ mA}\cdot\text{mg}^{-1}_{\text{Pt}}$ ), respectively. In addition, the mass-normalized and area-normalized peak current intensity of different catalysts toward MOR at 0.9 V vs RHE in acidic and alkaline media are also summarized in Figures 7e and f to further evaluate the MOR activity of different catalysts. Clearly, the Pt/ $Ti_{0.5}Cr_{0.5}N$ /G catalysts have not only the highest mass activity but also the highest area activity in comparison with those of the Pt/CrN/G, Pt/TiN/G, graphene free Pt/ $Ti_{0.5}Cr_{0.5}N$ , Pt/G, and commercial Pt/C catalysts. The area-normalized activities of the Pt/ $Ti_{0.5}Cr_{0.5}N$ /G catalyst in the positive direction are 1.01 and  $1.41 \text{ mA}\cdot\text{cm}^{-2}_{\text{Pt}}$  in acidic and alkaline media, respectively (Table 4). Such results suggest that the combination of TiN with CrN to form a binary  $Ti_{0.5}Cr_{0.5}N$  solid solution and

loading TMN onto a graphene surface are both beneficial for improving catalytic performance.<sup>38</sup> Meanwhile, the onset potential is another important parameter for assessing the electrochemical catalytic activity of catalysts. The Pt/ $Ti_{0.5}Cr_{0.5}N$ /G catalyst displays the lowest onset potential, suggesting that it is more favorable for MOR (Figure 8b).<sup>54</sup> Furthermore, the ratio of the forward oxidation current density to the backward current density ( $I_f/I_b$ ) is an important indicator to describe the tolerance of the catalysts to the carbonaceous species.<sup>61,62</sup> It can be seen from Figure 7c and Table 4 that the  $I_f/I_b$  values are in the order of Pt/ $Ti_{0.5}Cr_{0.5}N$ /G (1.16) > Pt/ $Ti_{0.5}Cr_{0.5}N$  (1.07) > Pt/CrN/G (1.05) > Pt/TiN/G (1.09) > Pt/G (1.07) > Pt/C (0.88), suggesting that methanol can be more effectively oxidized on Pt/TMN/G catalysts during the forward potential scan, generating less poisoning species compared with Pt/C. As reported in the literature,<sup>63,64</sup> the difference in activity between alkaline and acid media may be rooted in two reasons: first, the reaction pathways were different in alkaline and acid media. During the reaction, methanol is first adsorbed on a suitable surface, and after that it may suffer diverse dehydrogenation steps. In this sense, methanol could be dehydrogenated to form adsorbed CO. Then, CO can be fully oxidized to  $CO_2$  in acidic media or to carbonate in alkaline media. Second, the catalyst surfaces may be distinct in alkaline and acid media. Oxygenated species may be generated on the surface of Pt/TMN/G catalysts in alkaline media. In addition to the activity, the stability of Pt/TMN/G catalysts is also an important feature for its application. Therefore, a long time test was carried out in solutions of both 1.0 M  $CH_3OH$  + 0.5 M  $H_2SO_4$  and 1.0 M  $CH_3OH$  + 0.1 M KOH and recorded at 0.93 V vs RHE to evaluate the catalytic stability and tolerance of CO intermediates of different catalysts by chronoamperometry measurements (Figures 7g and h). As seen in Figures 7g and h, the  $i-t$  curves of all catalysts decay rapidly at the initial stage, which might be due to the hydrogen adsorption and double-layer discharge, and then decay slowly due to the poisoning effect by slow adsorption of CO or CO-like intermediates on the catalyst surface.<sup>38,54</sup> After 10 000 s continuous measurements, the current densities for MOR on the Pt/ $Ti_{0.5}Cr_{0.5}N$ /G, Pt/ $Ti_{0.5}Cr_{0.5}N$ , Pt/CrN/G, Pt/TiN/G, Pt/G, and Pt/C catalysts were maintained at  $\sim 56, 47, 40, 38, 25,$  and  $32 \text{ mA}\cdot\text{mg}^{-1}_{\text{Pt}}$ , respectively, in acidic media. In alkaline media, the decreasing rates of current densities are lower than those in acidic media, indicating that these catalysts possess higher catalytic stability in alkaline media. As seen in Figure 7h, after 10 000 s continuous measurements, the current densities for MOR on the Pt/ $Ti_{0.5}Cr_{0.5}N$ /G, Pt/CrN/G, Pt/TiN/G, and Pt/C catalysts were maintained at  $\sim 132, 73, 47,$  and  $59 \text{ mA}\cdot\text{mg}^{-1}_{\text{Pt}}$ , respectively. Among these six catalysts, the Pt/ $Ti_{0.5}Cr_{0.5}N$ /G catalyst exhibits the highest stable current density, confirming its excellent catalytic stability and tolerance to CO intermediates toward MOR in both acidic and alkaline media. In addition, the electrocatalytic performance of other Pt/TMN/G catalysts (Pt/ $Mo_2N$ /G, Pt/ $Mo_{0.2}Ti_{0.8}N$ /G, Pt/WN/G, and Pt/ $W_{0.2}Ti_{0.8}N$ /G) were also evaluated using the MOR as a model reaction (Figure S13). These catalysts all displayed catalytic performance better than that of the Pt/C catalyst. Meanwhile, binary-Pt/TMN/G catalysts exhibited catalytic activity superior to that of the mono-Pt/TMN/G catalyst.

To further investigate the electrocatalytic performance of Pt/TMN/G, Pt/ $Ti_{0.5}Cr_{0.5}N$ , Pt/G, Pt/C, and graphene catalysts and the ORR activity and kinetics of the Pt/TiN/G, Pt/

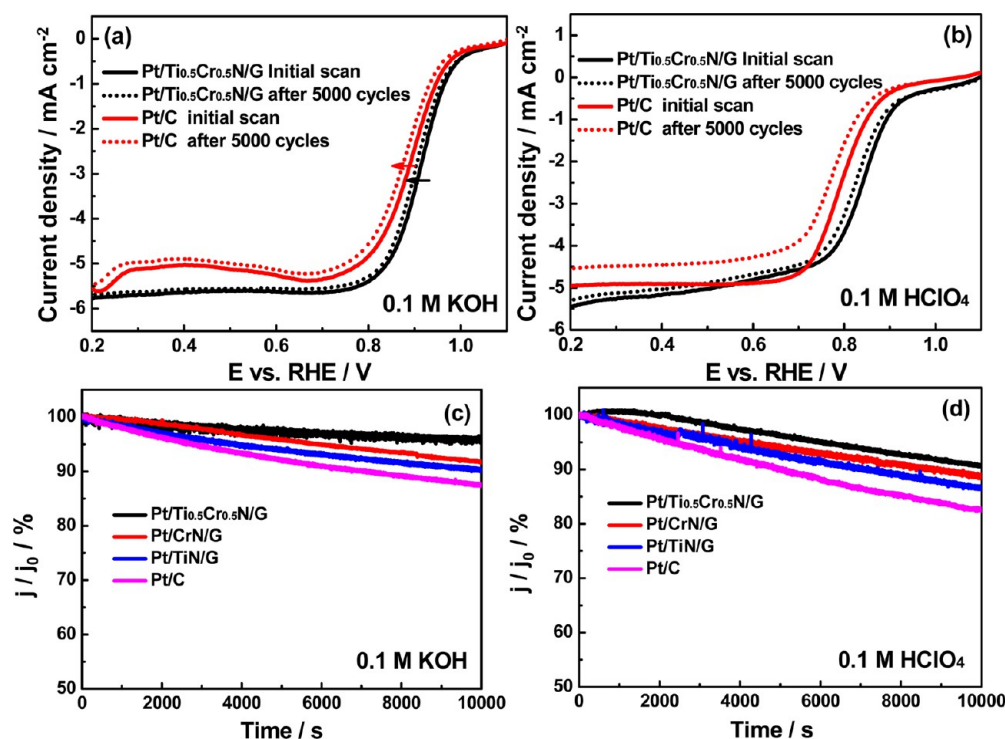


**Figure 9.** (a and b) RDE polarization curves of Pt/Ti<sub>0.5</sub>Cr<sub>0.5</sub>N/G and Pt/C before and after the stability test in O<sub>2</sub>-saturated 0.1 M KOH and HClO<sub>4</sub> media, respectively. (c and d) Current–time chronoamperometric responses of Pt/Ti<sub>0.5</sub>Cr<sub>0.5</sub>N/G, Pt/CrN/G, Pt/TiN, and Pt/C at 0.5 V. vs RHE in O<sub>2</sub>-saturated 0.1 M KOH and HClO<sub>4</sub> media, respectively, at a rotating speed of 900 rpm.

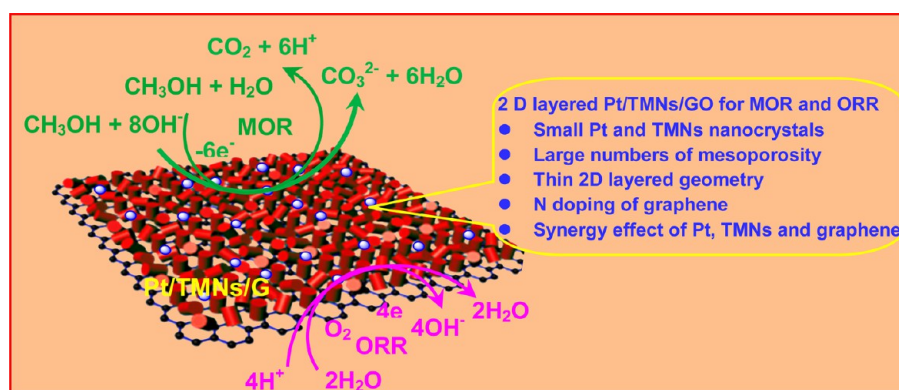
Ti<sub>0.5</sub>Cr<sub>0.5</sub>N/G, Pt/CrN/G, Pt/Ti<sub>0.5</sub>Cr<sub>0.5</sub>N, Pt/G, Pt/C, and graphene catalysts at the same mass loading content, a rotating-disk electrode (RDE) technique was used in 0.1 M KOH and 0.1 M HClO<sub>4</sub> media at room temperature. The LSV polarization curves for ORR show that the onset potentials of the Pt/TiN/G, Pt/Ti<sub>0.5</sub>Cr<sub>0.5</sub>N/G, Pt/CrN/G, Pt/Ti<sub>0.5</sub>Cr<sub>0.5</sub>N, Pt/bulk-Ti<sub>0.5</sub>Cr<sub>0.5</sub>N/G, Pt/C, and graphene catalysts are 0.97, 1.02, 0.98, 1.01, 0.98, 1.00, and 0.80 V vs RHE, respectively, and the corresponding half-wave potentials are 0.87, 0.91, 0.87, 0.90, 0.88, 0.89, and 0.70 V vs RHE, respectively, in 0.1 M KOH media (Figures 8a and b). Clearly, the ORR activity is increased following the order of graphene < Pt/TiN/G ≈ Pt/CrN/G < Pt/bulk-Ti<sub>0.5</sub>Cr<sub>0.5</sub>N/G < Pt/C < Pt/Ti<sub>0.5</sub>Cr<sub>0.5</sub>N < Pt/Ti<sub>0.5</sub>Cr<sub>0.5</sub>N/G, and the Pt/Ti<sub>0.5</sub>Cr<sub>0.5</sub>N/G catalyst possesses the best electrocatalytic performance toward ORR in alkaline media. Generally, the ORR kinetics are more sluggish in acidic media than in alkaline media.<sup>65</sup> Therefore, the electrocatalytic activities of these catalysts for ORR in acidic media (0.1 M HClO<sub>4</sub>) were also studied. The results reveal that all catalysts display excellent electrocatalytic activity, and their ORR activities follow the same order as that in alkaline media. The above results indicate that the Pt/Ti<sub>0.5</sub>Cr<sub>0.5</sub>N/G catalyst possesses excellent ORR activity in both alkaline and acidic media, and the significantly improved ORR activity of the Pt/Ti<sub>0.5</sub>Cr<sub>0.5</sub>N/G catalyst may be rooted in the combined function of TMN, graphene, and the mesoporous structure. In particular, the TMN may play a vital role in improving the ORR activity of the Pt/TMN/G catalyst.

To gain further insight into the ORR kinetics and catalytic mechanism, RDE polarization curves of the Pt/Ti<sub>0.5</sub>Cr<sub>0.5</sub>N/G catalyst were performed in the potential range of 0.2–1.1 V at 400–2400 rpm in alkaline (Figures 8c and d) and acidic media (Figures 8e and f). The limiting current density decreases from

6.49 to 3.20 mA·cm<sup>-2</sup> in 0.1 M KOH and from 6.99 to 3.35 mA·cm<sup>-2</sup> in 0.1 M HClO<sub>4</sub> as the rotating speed decreases from 2500 to 400 rpm because the diffusion distance of the O<sub>2</sub>-saturated electrolyte is shortened at high speeds.<sup>66</sup> The corresponding Koutecky–Levich (K–L) plots within the potential range from 0.3 to 0.6 V vs RHE show good linearity and parallelism in alkaline and acidic media (Figures 8d and f), which confirms that first-order reaction kinetics toward the oxygen concentration in the solution and the numbers of electrons transferred during the ORR are similar at different potentials.<sup>67</sup> Furthermore, the electron transfer numbers (*n*) are calculated from the slope of the K–L equation. For an alkaline electrolyte solution, the calculated value of *n* is approximately 4.07–4.21 in alkaline solution and 4.07–4.14 in acidic solution over the entire potential range, indicating that the ORR of the Pt/Ti<sub>0.5</sub>Cr<sub>0.5</sub>N/G catalyst fully follows the four-electron-transfer pathway, corresponding to the complete reduction of oxygen into water.

The stability of ORR catalysts is an important performance criterion. To assess the stability of the Pt/Ti<sub>0.5</sub>Cr<sub>0.5</sub>N/G catalyst, the accelerated durability test was first carried out by comparing the results with the Pt/C catalyst in 0.1 M KOH and 0.1 M HClO<sub>4</sub> media (Figures 9 a and b). Clearly, the polarization curves recorded after 5000 cyclic voltammograms display only a slightly negative shift of the half-wave potential of 10 mV in alkaline media and 14 mV in acidic media for the Pt/Ti<sub>0.5</sub>Cr<sub>0.5</sub>N/G catalyst. However, the half-wave potential negatively shifts by 14 mV in alkaline media and 20 mV in acidic media for the Pt/C catalyst. Meanwhile, diminishment of the diffusion-limited current for Pt/C is larger than that of the Pt/Ti<sub>0.5</sub>Cr<sub>0.5</sub>N/G catalyst. Then, the durability of Pt/TiN/G, Pt/CrN/G, Pt/Ti<sub>0.5</sub>Cr<sub>0.5</sub>N/G, and Pt/C for ORR was evaluated by continuous chronoamperometric measurements at vs RHE

**Scheme 2. Proposed Synergetic Mechanism for the Enhanced Catalytic Activity of the Mesoporous 2D Layered Pt/TMN/G Catalyst for the MOR and ORR**



in an  $O_2$ -saturated 0.1 M KOH and 0.1 M  $HClO_4$  media. After reaction for 10 000 s, the Pt/TiN/G, Pt/CrN/G, Pt/ $Ti_{0.5}Cr_{0.5}N/G$ , and Pt/C catalysts exhibit different levels of performance attenuation with 90.3, 91.7, 96.1, and 87.2% and 86.4, 88.8, 90.7, and 82.5% of the relative current persisting in alkaline and acidic media, respectively (Figures 9c and d). Obviously, the current density of the Pt/ $Ti_{0.5}Cr_{0.5}N/G$  catalyst had the smallest loss, and the loss was only 3.9% in alkaline media and 9.3% in acidic media. However, the current density of the Pt/C catalyst had a much greater loss, especially in acidic media, and the current loss reached 12.8% in alkaline media and 17.5% in acidic media due to surface oxidization, particle dissolution/aggregation/Oswald ripening over time, and weak interactions with the carbon support.<sup>68</sup> The above results reveal that the Pt/ $Ti_{0.5}Cr_{0.5}N/G$  catalyst indeed possesses excellent durability, which may make it a promising candidate as a cathode catalyst to replace commercial Pt/C for direct methanol fuel cells in both acidic and alkaline media.

Obviously, the Pt/ $Ti_{0.5}Cr_{0.5}N/G$  catalyst exhibits the best electrochemical catalytic performance toward MOR and ORR. It mainly shows in the following three aspects: (a) the highest mass activity and specific activity toward MOR and the largest limiting current density towards ORR, (b) the lowered onset potential toward MOR and the highest onset potential and half-wave potential, and (c) the enhanced long-term stability and resistance to CO poisoning toward MOR and excellent durability in both acidic and alkaline media. The enhanced electrochemical catalytic performance probably results from several reasons, as seen in Scheme 2. First, the uniquely ordered mesoporous structure can effectively increase the specific surface areas and mass transfer efficiency of reactants and products, which is beneficial for the dispersion of Pt nanoparticles and further for the exposure of more active centers compared with those of nonporous Pt/G and Pt/C catalysts. Meanwhile, the confined effect of mesopores can effectively prevent the agglomeration of Pt nanoparticles during the electrocatalytic reaction and improve the stability of catalysts to some extent.<sup>69</sup> Second, the excellent conductivity and good chemical and electrochemical stability of  $Ti_{0.5}Cr_{0.5}N$  and the strong synergistic effect between Pt and  $Ti_{0.5}Cr_{0.5}N$  nanocrystals, which was proven by the XPS results, can effectively improve catalytic activity and stability.<sup>38</sup> Third, the composition of graphene with binary TMN can further enhance the electron-transport performance in Pt/TMN/G catalysts,<sup>34</sup> which is conducive to further improvement of electrocatalytic properties. Therefore, the catalytic activity of the Pt/

$Ti_{0.5}Cr_{0.5}N/G$  catalyst is higher than that of the graphene-free Pt/ $Ti_{0.5}Cr_{0.5}N$  catalyst. The EIS results confirm that the Pt/ $Ti_{0.5}Cr_{0.5}N/G$  catalyst possesses an electron-transport property superior to those of the Pt/ $Ti_{0.5}Cr_{0.5}N$  and Pt/C catalysts. Finally, the partial N-doping of graphene (pyridine-like N proven by XPS spectrum of N 1s) in the Pt/TMN/G catalysts may also be beneficial for the improvement of electrocatalytic performance.<sup>50</sup> Thus, it can be asserted that the outstanding electrocatalytic activity of Pt/ $Ti_{0.5}Cr_{0.5}N/G$  catalysts stems from their superiority in unique building architecture. Moreover, the nanocomposites of graphene with mesoporous TMN can be expanded to other material systems to improve their performance in many fields of electrocatalysis, photocatalysis, sensors, and so forth.

#### 4. CONCLUSION

A facile, efficient, and general nanocasting method was developed for constructing a series of 2D layered mesoporous transition-metal nitride/graphene nanocomposites with large surface areas and very small TMN embedded in graphene nanosheets. After being decorating with Pt nanoparticles, the obtained 2D layered mesoporous Pt/TMN/G catalysts displayed excellent catalytic activity and durability for MOR and ORR. Noticeably, the binary Pt/ $Ti_{0.5}Cr_{0.5}N/G$  catalyst exhibited the best electrocatalytic performance compared to the performances of the mono-Pt/TMN/G, Pt/C, and Pt/G catalysts. This improved performance is due to its large specific surface area, high porosity, and strong interactions of Pt,  $Ti_{0.5}Cr_{0.5}N$ , and graphene that allows faster oxidation of the CO produced by methanol oxidation and excellent electron transfer property of the Pt/ $Ti_{0.5}Cr_{0.5}N/G$  catalyst. The confinement effect of mesopores existing in the Pt/ $Ti_{0.5}Cr_{0.5}N/G$  catalyst can effectively inhibit the aggregation of Pt nanoparticles during the operation process, thereby resulting in enhanced stability. It can be inferred that  $Ti_{0.5}Cr_{0.5}N/G$  can be used as a promising support to improve Pt activity and durability for electrocatalytic reactions in both alkaline and acidic media. Our work provides an effective and robust route to design various mesoporous binary transition-metal nitride/graphene nanocomposites which can be used as the support for Pt-based catalysts that can be applied in PEMFCs.

#### ■ ASSOCIATED CONTENT

##### Supporting Information

The Supporting Information is available free of charge on the ACS Publications website at DOI: 10.1021/acsami.6b03747.

SEM images of KIT-6/G template and various 2D layered mesoporous Pt/TMN/G catalysts, XRD patterns of graphene oxide, Pt/C, Pt/TMN/G, and Pt/G catalysts and various 2D layered mesoporous TMN/G supports, TEM images of bulk Pt/TiN catalyst and various 2D layered mesoporous TMN/G supports, XPS data of 2D layered mesoporous TiN/G, Cr<sub>0.5</sub>Ti<sub>0.5</sub>N/G, and CrN/G supports, N<sub>2</sub> adsorption–desorption isotherms and pore size distribution of 2D layered mesoporous Pt/Mo<sub>2</sub>N/G, Pt/WN/G, Pt/Ti<sub>0.8</sub>Mo<sub>0.2</sub>N/G, and Pt/Ti<sub>0.8</sub>W<sub>0.2</sub>N/G catalysts, cyclic voltammetry of Pt (~5 wt %)/Cr<sub>0.5</sub>Ti<sub>0.5</sub>N/G, Pt (~10 wt %)/Cr<sub>0.5</sub>Ti<sub>0.5</sub>N/G, and Pt (~20 wt %)/Cr<sub>0.5</sub>Ti<sub>0.5</sub>N/G catalysts in a 1 M CH<sub>3</sub>OH/0.5 M H<sub>2</sub>SO<sub>4</sub> solution, and cyclic voltammetry and chronoamperometry curves of 2D layered mesoporous Pt/Mo<sub>2</sub>N/G, Pt/WN/G, Pt/Ti<sub>0.8</sub>Mo<sub>0.2</sub>N/G, and Pt/Ti<sub>0.8</sub>W<sub>0.2</sub>N/G catalysts (PDF)

## AUTHOR INFORMATION

### Corresponding Authors

\*E-mail: cejzhang@imu.edu.cn.

\*E-mail: sirui@sinap.ac.cn.

### Notes

The authors declare no competing financial interest.

## ACKNOWLEDGMENTS

J.Z. thanks the funding support from NSFC (Grant 21261011), Application Program from Inner Mongolia Science and Technology Department (Grant 2016), and the Program for New Century Excellent Talents in University (Grant NCET-10-0907). R.S. thanks the funding support from NSFC (Grant 21373259) and the Hundred Talents project, Strategic Priority Research Program of the Chinese Academy of Sciences (Grant XDA09030102). B.C.L. thanks the funding support from Program of Higher-level Talents of Inner Mongolia University (Grant 21300-5155105).

## REFERENCES

- (1) Steele, B. C. H.; Heinzel, A. Materials for Fuel-Cell Technologies. *Nature* **2001**, *414*, 345–352.
- (2) Bruce, P. G.; Hardwick, L. J.; Abraham, K. M. Lithium-Air and Lithium-Sulfur Batteries. *MRS Bull.* **2011**, *36*, 506–512.
- (3) Orilall, M. C.; Matsumoto, F.; Zhou, Q.; Sai, H.; Abruna, H. D.; DiSalvo, F. J.; Wiesner, U. One-Pot Synthesis of Platinum-Based Nanoparticles Incorporated into Mesoporous Niobium Oxide-Carbon Composites for Fuel Cell Electrodes. *J. Am. Chem. Soc.* **2009**, *131*, 9389–9395.
- (4) Chen, C.; Kang, Y. J.; Huo, Z. Y.; Zhu, Z. W.; Huang, W. Y.; Xin, H. L. L.; Snyder, J. D.; Li, D. G.; Herron, J. A.; Mavrikakis, M.; Chi, M. F.; More, K. L.; Li, Y. D.; Markovic, N. M.; Somorjai, G. A.; Yang, P. D.; Stamenkovic, V. R. Highly Crystalline Multimetallic Nanoframes with Three-Dimensional Electrocatalytic Surfaces. *Science* **2014**, *343*, 1339–1343.
- (5) Borup, R.; Meyers, J.; Pivovar, B.; Kim, Y. S.; Mukundan, R.; Garland, N.; Myers, D.; Wilson, M.; Garzon, F.; Wood, D.; Zelenay, P.; More, K.; Stroh, K.; Zawodzinski, T.; Boncella, J.; McGrath, J. E.; Inaba, M.; Miyatake, K.; Hori, M.; Ota, K.; Ogumi, Z.; Miyata, S.; Nishikata, A.; Siroma, Z.; Uchimoto, Y.; Yasuda, K.; Kimijima, K. I.; Iwashita, N. Scientific Aspects of Polymer Electrolyte Fuel Cell Durability and Degradation. *Chem. Rev.* **2007**, *107*, 3904–3951.
- (6) Cao, M. N.; Wu, D. S.; Cao, R. Recent Advances in the Stabilization of Platinum Electrocatalysts for Fuel-Cell Reactions. *ChemCatChem* **2014**, *6*, 26–45.
- (7) Li, F. H.; Guo, Y. Q.; Li, R. Q.; Wu, F.; Liu, Y.; Sun, X. Y.; Li, C. B.; Wang, W.; Gao, J. P. A Facile Method to Synthesize Supported Pd–Au Nanoparticles using Graphene Oxide as the Reductant and their Extremely High Electrocatalytic Activity for the Electrooxidation of Methanol and Ethanol. *J. Mater. Chem. A* **2013**, *1*, 6579–6587.
- (8) Bing, Y. H.; Liu, H. S.; Zhang, L.; Ghosh, D.; Zhang, J. J. Nanostructured Pt-Alloy Electrocatalysts for PEM Fuel Cell Oxygen Reduction Reaction. *Chem. Soc. Rev.* **2010**, *39*, 2184–2202.
- (9) Tan, Y. M.; Xu, C. F.; Chen, G. X.; Fang, X. L.; Zheng, N. F.; Xie, Q. J. Facile Synthesis of Manganese-Oxide-Containing Mesoporous Nitrogen-Doped Carbon for Efficient Oxygen Reduction. *Adv. Funct. Mater.* **2012**, *22*, 4584–4591.
- (10) Ma, X. M.; Meng, H.; Cai, M.; Shen, P. K. Bimetallic Carbide Nanocomposite Enhanced Pt Catalyst with High Activity and Stability for the Oxygen Reduction Reaction. *J. Am. Chem. Soc.* **2012**, *134*, 1954–1957.
- (11) Chen, Z. W.; Higgins, D.; Yu, A. P.; Zhang, L.; Zhang, J. J. A Review on Non-Precious Metal Electrocatalysts for PEM Fuel Cells. *Energy Environ. Sci.* **2011**, *4*, 3167–3192.
- (12) Wang, Y. J.; Wilkinson, D. P.; Zhang, J. J. Noncarbon Support Materials for Polymer Electrolyte Membrane Fuel Cell Electrocatalysts. *Chem. Rev.* **2011**, *111*, 7625–7651.
- (13) Walcarius, A. Mesoporous Materials and Electrochemistry. *Chem. Soc. Rev.* **2013**, *42*, 4098–4140.
- (14) Zhang, C. W.; Xu, L. B.; Shan, N. N.; Sun, T. T.; Chen, J. F.; Yan, Y. S. Enhanced Electrocatalytic Activity and Durability of Pt Particles Supported on Ordered Mesoporous Carbon Spheres. *ACS Catal.* **2014**, *4*, 1926–1930.
- (15) Huang, H. J.; Wang, X. Recent Progress on Carbon-Based Support Materials for Electrocatalysts of Direct Methanol Fuel Cells. *J. Mater. Chem. A* **2014**, *2*, 6266–6291.
- (16) Yuan, W. Y.; Lu, S. F.; Xiang, Y.; Jiang, S. P. Pt-Based Nanoparticles on Non-Covalent Functionalized Carbon Nanotubes as Effective Electrocatalysts for Proton Exchange Membrane Fuel Cells. *RSC Adv.* **2014**, *4*, 46265–46284.
- (17) Nassr, A. A. A.; Sinev, I.; Pohl, M. M.; Grunert, W.; Bron, M. Rapid Microwave-Assisted Polyol Reduction for the Preparation of Highly Active PtNi/CNT Electrocatalysts for Methanol Oxidation. *ACS Catal.* **2014**, *4*, 2449–2462.
- (18) Zhou, X. J.; Qiao, J. L.; Yang, L.; Zhang, J. J. A Review of Graphene-Based Nanostructural Materials for Both Catalyst Supports and Metal-Free Catalysts in PEM Fuel Cell Oxygen Reduction Reactions. *Adv. Energy Mater.* **2014**, *4*, 1301523.
- (19) Antolini, E. Graphene as a New Carbon Support for Low-Temperature Fuel Cell Catalysts. *Appl. Catal., B* **2012**, *123*, 52–68.
- (20) Qiu, H. J.; Zou, F. X. Nanoporous PtCo Surface Alloy Architecture with Enhanced Properties for Methanol Electrooxidation. *ACS Appl. Mater. Interfaces* **2012**, *4*, 1404–1410.
- (21) Debe, M. K. Electrocatalyst Approaches and Challenges for Automotive Fuel Cells. *Nature* **2012**, *486*, 43–51.
- (22) Zhong, H. X.; Chen, X. B.; Zhang, H. M.; Wang, M. R.; Mao, S. S. Proton Exchange Membrane Fuel Cells with Chromium Nitride Nanocrystals as Electrocatalysts. *Appl. Phys. Lett.* **2007**, *91*, 163103.
- (23) Avasarala, B.; Murray, T.; Li, W. Z.; Haldar, P. Titanium Nitride Nanoparticles Based Electrocatalysts for Proton Exchange Membrane Fuel Cells. *J. Mater. Chem.* **2009**, *19*, 1803–1805.
- (24) Yang, M. H.; Cui, Z. M.; DiSalvo, F. J. Mesoporous Titanium Nitride Supported Pt Nanoparticles as High Performance Catalysts for Methanol Electrooxidation. *Phys. Chem. Chem. Phys.* **2013**, *15*, 1088–1092.
- (25) Yang, M. H.; Cui, Z. M.; DiSalvo, F. J. Mesoporous Chromium Nitride as a High Performance Non-Carbon Support for the Oxygen Reduction Reaction. *Phys. Chem. Chem. Phys.* **2013**, *15*, 7041–7044.
- (26) Yang, M. H.; Guarecuco, R.; DiSalvo, F. J. Mesoporous Chromium Nitride as High Performance Catalyst Support for Methanol Electrooxidation. *Chem. Mater.* **2013**, *25*, 1783–1787.
- (27) Yang, Y. M.; Liu, J.; Han, Y. Z.; Huang, H.; Liu, N. Y.; Liu, Y.; Kang, Z. H. Porous Cobalt, Nitrogen-Co doped Carbon Nanostructures from Carbon Quantum Dots and VB12 and their Catalytic

Properties for Oxygen Reduction. *Phys. Chem. Chem. Phys.* **2014**, *16*, 25350–25357.

(28) Yan, X. H.; Xu, B. Q. Mesoporous Carbon Material Co-Doped with Nitrogen and Iron (Fe–N–C): High-Performance Cathode Catalyst for Oxygen Reduction Reaction in Alkaline Electrolyte. *J. Mater. Chem. A* **2014**, *2*, 8617–8622.

(29) Yan, H. J.; Tian, C. G.; Sun, L.; Wang, B.; Wang, L.; Yin, J.; Wu, A. P.; Fu, H. G. Small-Sized and High-Dispersed WN from  $[\text{SiO}_4(\text{W}_3\text{O}_9)_4]^{4-}$  Clusters Loading on GO-Derived Graphene as Promising Carriers for Methanol Electro-oxidation. *Energy Environ. Sci.* **2014**, *7*, 1939–1949.

(30) Qi, L.; Yin, Y.; Shi, W. Y.; Liu, J. G.; Xing, D. M.; Liu, F. Q.; Hou, Z. J.; Gu, J.; Ming, P. W.; Zou, Z. Intermittent Microwave Synthesis of Nanostructured Pt/TiN–Graphene with High Catalytic Activity for Methanol Oxidation. *Int. J. Hydrogen Energy* **2014**, *39*, 16036–16042.

(31) Liu, M. J.; Dong, Y. Z.; Wu, Y. M.; Feng, H. B.; Li, J. H. Titanium Nitride Nanocrystals on Nitrogen-Doped Graphene as an Efficient Electrocatalyst for Oxygen Reduction Reaction. *Chem. - Eur. J.* **2013**, *19*, 14781–14786.

(32) Liu, M. M.; Zhang, R. Z.; Chen, W. Graphene-Supported Nanoelectrocatalysts for Fuel Cells: Synthesis, Properties, and Applications. *Chem. Rev.* **2014**, *114*, 5117–5160.

(33) Wen, Z. H.; Cui, S. M.; Pu, H. H.; Mao, S.; Yu, K. H.; Feng, X. L.; Chen, J. H. Metal Nitride/Graphene Nanohybrids: General Synthesis and Multifunctional Titanium Nitride/Graphene Electrocatalyst. *Adv. Mater.* **2011**, *23*, 5445–5450.

(34) Yue, Y. H.; Han, P. X.; He, X.; Zhang, K. J.; Liu, Z. H.; Zhang, C. J.; Dong, S. M.; Gu, L.; Cui, G. L. In situ Synthesis of a Graphene/Titanium Nitride Hybrid Material with Highly Improved Performance for Lithium Storage. *J. Mater. Chem.* **2012**, *22*, 4938–4943.

(35) Xiao, Y. H.; Fu, Z. G.; Zhan, G. H.; Pan, Z. C.; Xiao, C. M.; Wu, S. K.; Chen, C.; Hu, G. H.; Wei, Z. G. Increasing Pt Methanol Oxidation Reaction Activity and Durability with a Titanium Molybdenum Nitride Catalyst Support. *J. Power Sources* **2015**, *273*, 33–40.

(36) Zhao, W. T.; DiSalvo, F. J. Direct Access to Macroporous Chromium Nitride and Chromium Titanium Nitride with Inverse Opal Structure. *Chem. Commun.* **2015**, *51*, 4876–4879.

(37) Xiao, Y. H.; Zhan, G. H.; Fu, Z. G.; Pan, Z. C.; Xiao, C. M.; Wu, S. K.; Chen, C.; Hu, G. H.; Wei, Z. G. Titanium Cobalt Nitride Supported Platinum Catalyst with High Activity and Stability for Oxygen Reduction Reaction. *J. Power Sources* **2015**, *284*, 296–304.

(38) Cui, Z. M.; Yang, M. H.; DiSalvo, F. J. Mesoporous  $\text{Ti}_{10}\text{S}\text{Cr}_{0.5}\text{N}$  supported PdAg Nanoalloy as Highly Active and Stable Catalysts for the Electro-oxidation of Formic Acid and Methanol. *ACS Nano* **2014**, *8*, 6106–6113.

(39) Lee, C. W.; Roh, K. C.; Kim, K. B. A Highly Ordered Cubic Mesoporous Silica/Graphene Nanocomposite. *Nanoscale* **2013**, *5*, 9604–9608.

(40) Hui, Z. Z.; Tang, X. W.; Wei, R. H.; Hu, L.; Yang, J.; Luo, H. M.; Dai, J. M.; Song, W. H.; Liu, X. Z.; Zhu, X. B.; Sun, Y. P. Facile Chemical Solution Deposition of Nanocrystalline CrN Thin Films with Low Magnetoresistance. *RSC Adv.* **2014**, *4*, 12568–12571.

(41) Liu, B. C.; Yu, S. L.; Wang, Q.; Hu, W. T.; Jing, P.; Liu, Y.; Jia, W. J.; Liu, Y. X.; Liu, L. X.; Zhang, J. Hollow Mesoporous Ceria Nanoreactors with Enhanced Activity and Stability for Catalytic Application. *Chem. Commun.* **2013**, *49*, 3757–3759.

(42) Villa, K.; Murcia-Lopez, S.; Andreu, T.; Morante, J. R. Mesoporous  $\text{WO}_3$  Photocatalyst For the Partial Oxidation of Methane to Methanol using Electron Scavengers. *Appl. Catal., B* **2015**, *163*, 150–155.

(43) Tuysuz, H.; Weidenthaler, C.; Grewe, T.; Salabas, E. L.; Romero, M. J. B.; Schuth, F. A Crystal Structure Analysis and Magnetic Investigation on Highly Ordered Mesoporous  $\text{Cr}_2\text{O}_3$ . *Inorg. Chem.* **2012**, *51*, 11745–11752.

(44) Ma, L. A.; Zhao, X. A.; Si, F. Z.; Liu, C. P.; Liao, J. H.; Liang, L. A.; Xing, W. A Comparative Study of Pt/C and Pt– $\text{MoO}_x$ /C Catalysts

with Various Compositions for Methanol Electro-oxidation. *Electrochim. Acta* **2010**, *55*, 9105–9112.

(45) Yan, Z. X.; He, G. Q.; Shen, P. K.; Luo, Z. B.; Xie, J. M.; Chen, M. MoC–Graphite Composite as a Pt Electrocatalyst Support for Highly Active Methanol Oxidation and Oxygen Reduction Reaction. *J. Mater. Chem. A* **2014**, *2*, 4014–4022.

(46) Wang, C.; Daimon, H.; Sun, S. Dumbbell-Like Pt– $\text{Fe}_3\text{O}_4$  Nanoparticles and their Enhanced Catalysis for Oxygen Reduction Reaction. *H. Nano Lett.* **2009**, *9*, 1493–1496.

(47) Xiao, Y.; Zhan, G.; Fu, Z.; Pan, Z.; Xiao, C.; Wu, S.; Chen, C.; Hu, G.; Wei, Z. Robust Non-Carbon Titanium Nitride Nanotubes Supported Pt Catalyst with Enhanced Catalytic Activity and Durability for Methanol Oxidation Reaction. *Electrochim. Acta* **2014**, *141*, 279–285.

(48) Roca-Ayats, M.; García, G.; Galante, J. L.; Peña, M. A.; Martínez-Huerta, M. V. TiC, TiCN, and TiN Supported Pt Electrocatalysts for CO and Methanol Oxidation in Acidic and Alkaline Media. *J. Phys. Chem. C* **2013**, *117*, 20769–20777.

(49) Zhao, Y.; Wang, Y.; Dong, L.; Zhang, Y.; Huang, J.; Zang, J.; Lu, J.; Xu, X. Core-Shell Structural Nanodiamond@TiN Supported Pt Nanoparticles as a Highly Efficient and Stable Electrocatalyst for Direct Methanol Fuel Cells. *Electrochim. Acta* **2014**, *148*, 8–14.

(50) Jia, Y. D.; Wang, Y. H.; Dong, L.; Huang, J. J.; Zhang, Y.; Su, J.; Zang, J. B. A hybrid of Titanium Nitride and Nitrogen-Doped Amorphous Carbon Supported on SiC as a Noble Metal-free Electrocatalyst for Oxygen Reduction Reaction. *Chem. Commun.* **2015**, *51*, 2625–2628.

(51) Hasegawa, G.; Kitada, A.; Kawasaki, S.; Kanamori, K.; Nakanishi, K.; Kobayashi, Y.; Kageyama, H.; Abe, T. Impact of Electrolyte on Pseudocapacitance and Stability of Porous Titanium Nitride (TiN) Monolithic Electrode. *J. Electrochem. Soc.* **2015**, *162*, A77–A85.

(52) Saha, N. C.; Tompkins, H. G. Titanium Nitride Oxidation Chemistry: An X-ray Photoelectron Spectroscopy Study. *J. Appl. Phys.* **1992**, *72*, 3072–3079.

(53) Lippitz, A.; Hubert, T. XPS Investigations of Chromium Nitride Thin Films. *Surf. Coat. Technol.* **2005**, *200*, 250–253.

(54) Ding, L. X.; Wang, A. L.; Li, G. R.; Liu, Z. Q.; Zhao, W. X.; Su, C. Y.; Tong, Y. X. Porous Pt–Ni–P Composite Nanotube Arrays: Highly Electroactive and Durable Catalysts for Methanol Electro-oxidation. *J. Am. Chem. Soc.* **2012**, *134*, 5730–5733.

(55) Frenkel, A. I.; Hills, C. W.; Nuzzo, R. G. A View from the Inside: Complexity in the Atomic Scale Ordering of Supported Metal Nanoparticles. *J. Phys. Chem. B* **2001**, *105*, 12689–12703.

(56) Sun, T.; Xu, L.; Yan, Y.; Zakhidov, A. A.; Baughman, R. H.; Chen, J. Ordered Mesoporous Nickel Sphere Arrays for Highly Efficient Electrocatalytic Water Oxidation. *ACS Catal.* **2016**, *6*, 1446–1450.

(57) Lv, C.; Peng, Z.; Zhao, Y.; Huang, Z.; Zhang, C. The Hierarchical Nanowires Array of Iron Phosphide Integrated on a Carbon Fiber Paper as an Effective Electrocatalyst for Hydrogen Generation. *J. Mater. Chem. A* **2016**, *4*, 1454–1460.

(58) Liu, L.; Zhang, H.; Mu, Y.; Yang, J.; Wang, Y. Porous Iron Cobaltate Nanoneedles Array on Nickel Foam as Anode Materials for Lithium-ion Batteries with Enhanced Electrochemical Performance. *ACS Appl. Mater. Interfaces* **2016**, *8*, 1351–1359.

(59) Zhang, G. G.; Zhang, M. W.; Ye, X. X.; Qiu, X. Q.; Lin, S.; Wang, X. C. Iodine Modified Carbon Nitride Semiconductors as Visible Light Photocatalysts for Hydrogen Evolution. *Adv. Mater.* **2014**, *26*, 805–809.

(60) Hou, Y.; Wen, Z. H.; Cui, S. M.; Guo, X. R.; Chen, J. H. Constructing 2D Porous Graphitic  $\text{C}_3\text{N}_4$  Nanosheets/Nitrogen-Doped Graphene/Layered  $\text{MoS}_2$  Ternary Nanojunction with Enhanced Photoelectrochemical Activity. *Adv. Mater.* **2013**, *25*, 6291–6297.

(61) Yang, S. B.; Gong, Y. J.; Zhang, J. S.; Zhan, L.; Ma, L. L.; Fang, Z. Y.; Vajtai, R.; Wang, X. C.; Ajayan, P. M. Carbon Nanotube-Based Tandem Absorber with Tunable Spectral Selectivity: Transition from

Near-Perfect Blackbody Absorber to Solar Selective Absorber. *Adv. Mater.* **2013**, *25*, 2452–2456.

(62) Liu, X. J.; Cui, C. H.; Gong, M.; Li, H. H.; Xue, Y.; Fan, F. J.; Yu, S. H. Pt–Ni Alloyed Nanocrystals with Controlled Architectures for Enhanced Methanol Oxidation. *Chem. Commun.* **2013**, *49*, 8704–8706.

(63) Roca-Ayats, M.; García, G.; Galante, J. L.; Peña, M. A.; Martínez-Huerta, M. V. TiC, TiCN, and TiN Supported Pt Electrocatalysts for CO and Methanol Oxidation in Acidic and Alkaline Media. *J. Phys. Chem. C* **2013**, *117*, 20769–20777.

(64) Guillén-Villafuerte, O.; García, G.; Guil-López, R.; Nieto, E.; Rodríguez, J. L.; Fierro, J. L. G.; Pastor, E. Carbon Monoxide and Methanol Oxidations on Pt/X@MoO<sub>3</sub>/C (X = Mo<sub>2</sub>C, MoO<sub>2</sub>, MoO) Electrodes at Different Temperatures. *J. Power Sources* **2013**, *231*, 163–172.

(65) Gu, S.; Xu, B.; Yan, Y. Electrochemical Energy Engineering: A New Frontier of Chemical Engineering Innovation. *Annu. Rev. Chem. Biomol. Eng.* **2014**, *5*, 429–454.

(66) Zhang, Y.; Chu, M.; Yang, L.; Deng, W.; Tan, Y.; Ma, M.; Xie, Q. Synthesis and Oxygen Reduction Properties of Three-Dimensional Sulfur-Doped Graphene Networks. *Chem. Commun.* **2014**, *50*, 6382–6385.

(67) Lai, L.; Potts, J. R.; Zhan, D.; Wang, L.; Poh, C. K.; Tang, C.; Gong, H.; Shen, Z.; Lin, J.; Ruoff, R. S. Exploration of the Active Center Structure of Nitrogen-Doped Graphene-Based Catalysts for Oxygen Reduction Reaction. *Energy Environ. Sci.* **2012**, *5*, 7936–7942.

(68) Wei, J.; Hu, Y.; Wu, Z.; Liang, Y.; Leong, S.; Kong, B.; Zhang, X.; Zhao, D.; Simon, G. P.; Wang, H. A Graphene-Directed Assembly Route to Hierarchically Porous Co–N<sub>x</sub>/C Catalysts for High-Performance Oxygen Reduction. *J. Mater. Chem. A* **2015**, *3*, 16867–16873.

(69) Yamauchi, Y.; Tonegawa, A.; Komatsu, M.; Wang, H. J.; Wang, L.; Nemoto, Y.; Suzuki, N.; Kuroda, K. Electrochemical Synthesis of Mesoporous Pt–Au Binary Alloys with Tunable Compositions for Enhancement of Electrochemical Performance. *J. Am. Chem. Soc.* **2012**, *134*, 5100–5109.